Effects of Droplet Size on Intrusion of Sub-Surface Oil Spills

by

Godine Kok Yan Chan

Submitted to the Department of Civil and Environmental Engineering
in partial fulfillment of the requirements for the degree of

Master of Science in Civil and Environmental Engineering

at the

MASSACHUSETTS INSTITUTE OF TECHNOLOGY

February 2013

Author .....
Department of Civil and Environmental Engineering
November 2, 2012

Certified by .....
E. Eric Adams
Senior Research Engineer and Lecturer of Civil and Environmental Engineering
Thesis Supervisor

Accepted by .....
Heidi Nepf
Chair, Departmental Committee for Graduate Students

Effects of Droplet Size on Intrusion of Sub-Surface Oil Spills

by

Godine Kok Yan Chan

Submitted to the Department of Civil and Environmental Engineering
On November 2, 2012, in partial fulfillment of the
requirements for the degree of
Master of Science in Civil and Environmental Engineering

Abstract

This thesis explores the effects of droplet size on droplet intrusion in sub-surface oil spills. Laboratory experiments were performed where glass beads of various sizes, which serve to simulate oil droplets in deepsea oil spills, were released vertically in a quiescent salinity stratified ambient and descended as multi-phase plumes. The two-tank stratification method was used to create linear density profiles for all experiments. The resulting radial concentration distributions of the dispersed phases were obtained by collecting the settled particles from the bottom of the tank. The radial distributions recorded were found to resemble Gaussian distributions, based on visual observations and analyses of kurtosis, which is consistent with particles being vertically well mixed in the intrusion layer. A new typology was proposed to describe plume structures with $U_N = u_s/(BN)^{1/4} \leq 1.4$. For $U_N \leq 1.4$ particle detrain from the plem, but only those with smallest slip velocity ($U_N \leq 0.3$) intrude. An analytical model assuming well-mixed particle distributions within the intrusion layer was also used to predict the spread of the particle distribution based on initial buoyancy flux B, stratification frequency N, the particle slip velocity u_s, and the non-dimensional slip velocity U_N. Comparison between experimental results and the analytical model suggested that the model accurately predicts the spread of the particles for $U_N \leq 1.4$. Experiments with beads of difference sizes also suggested that the interaction between two particle groups has minimal effects on their radial particle spread. This indicates that particles of difference sizes can be treated independently when analyzing their radial plume spread.

Chemical dispersants produce small oil droplets and the current experiments provide references on the minimum diameter needed for efficient particle spread (Type 1a* plume). By knowing the following parameters for a scenario - 1) initial buoyancy flux B; 2) the ambient stratification profile N; and 3) the slip velocities of the droplets u_s - suitable amounts of dispersant can be determined and applied to reduce the size of the particles exiting the spill, allowing them to intrude and spread for a larger distance in the ocean column. A hypothetical example with conditions taken from the 'Deep Spill' experiment and Deepwater Horizon oil spill was also presented for reference.

Thesis Supervisor: E. Eric Adams
Title: Senior Research Engineer and Lecturer of Civil and Environmental Engineering

Acknowledgments

This project was sponsored by the Chevron-MITei University Partnership Program, and my study at MIT was made possible by the National Science Foundation Graduate Research Fellowship Program.

Numerous people in and out of MIT contributed much to the success of this project. First and foremost, my advisor, Dr. E. Eric Adams provided me invaluable guidance and insight in this project. No words are enough to express my sincere gratitude for all his support and care throughout my study at MIT. His hospitability, together with his wife and family, let me have many cherishable Thanksgiving and Christmas memories. Also, I would like to thank Dr. Cort Cooper from Chevron for his involvement in this project. A number of current and graduated students in Parsons Lab made considerable contributions to my research as well. Special thanks go to Dr. Aaron Chow for his generous assistance amid his busy and hectic work schedule. I would also like to thank Ruo-Qian Wong and Natasha Maas in Adam's Lab for their remarkable insight in advancing my research. Special thanks also go to Prof. Heidi Nepf and her students, Mitul Luhar and Jeff Rominger, for providing me laboratory resources and assistance whilst doing experiments in the Environmental Fluids Lab. It should not go unsaid my appreciation to Prof. Adrian Law, Prof. Huang Zhenhua, Dr. Adrian Lai, and Zhao Bing and his wife for their hospitality during my stay at the National Technology University in Singapore.

And last but most important, thanks to my family, Mom, Dad and Godfrey, as well as my extended families for their endless love and countless support. Their counsel and encouragement give me strength to work for the best. I am also thankful to God for his blessings and guidance everyday in my journey. Finally, I would like to dedicate this work to my beloved grandmother Chan, who passed away during my first year of studies at MIT.

Contents

List of Figures

List of Tables

1. Background and Motivation

Human dependence on fossil fuel to provide energy for daily uses has been rising in the recent years. Demand for crude oil remains extremely high, and with lucrative profits as a constant motivator, oil companies continue to expand their reach and drill for riches in extreme territories such as freezing cold climate or deep treacherous seas. One of the astonishing technological advancements in modern engineering is the deep sea drilling platform, that allows oil companies to tap into unclaimed offshore oil fields and extract oil and gas buried deep below the sea floor. These operations are dangerous and come with many risks, one of which is a deepsea oil blowout, such event will damage the drilling structure, endanger lives working on the platform and release large amounts of oil and gases into the ocean column. An example of such tragic event was the BP Deepwater Horizon oil spill in 2010 which caused serious environmental and sociological problems in the Gulf of Mexico. Such a disastrous event reignites the drive to understand oil plumes released in deep ocean. Along with other multi-phase plume applications this provides strong incentive in studying the intrusion and particle spread of multi-phase plumes using laboratory scale experiments.

This thesis explores the effects of droplet sizes on intrusion of two-phase plumes. Laboratory experiments using glass beads were conducted in quiescent stratification for studying plume behavior. Experimental data were collected to understand how particles intrude and spread in stratification. In addition, these beads mimic oil droplets spilled from a deepsea oil blowout while they rise to the surface of the ocean, providing essential experimental data for decisions on the type and quantity of dispersion needed in an oil blowout scenario. Other applications of multi-phase plumes also benefits from the current experiments including bubble plumes for reservoir destratification, deep ocean carbon sequestration and sediment laden plumes that occur in nature.

1.1. Application of multi-phase plumes

1.1.1. Deep sea oil spills

The desire to tap into offshore oil fields in the Gulf of Mexico and other major oil fields around the world offer great incentive in predicting the fate of oil in case of accidental oil spill in the deep seas. Sources of spilled oil in such operations include damaged pipelines, sunken tankers

and oil well blowouts, among which oil blowouts are the most damaging and complicated (Yapa & Chen [53], Yapa et al. [54]). Deep sea oil blowouts occur when drilling encounters a region of high pressure fluids and fluids are allowed to travel uncontrollably towards the surface. Such events occurs when both the primary (natural layer including clay and sand surrounding the wellhead) and secondary (Blowout Prevention device) safety barriers are breached (Holland [23]). Oil blowouts are often disastrous due to inherit nature in which such events can occur. The locations of blowouts are often under high pressure and the points of release are through small cracks on the ocean floor or broken orifices, resulting in high exit velocities, flow rates and uncertain initial conditions of the mixture of oil and gases released from the reservoir. Blowouts can also last for a long period of time and release an enormous amount of oil and gas depending on the size of the oil field connected to the spill, causing timely and costly remediation efforts. Deepwater blowouts are catastrophic events that cause extensive damage to marine and wildlife habitats and fishing and tourism industries.

Topham [49] and McDougall [35] were two of the earliest researchers investigating the behavior of deepsea oil well blowouts. Topham [49] performed field experiments with air in 60 meters depth of seawater in an attempt to understand the hydrodynamics of oilwell blowouts. A few years later McDougall [35] devised an integral plume model based on laboratory experiments of stratified bubble plumes. McDougall proposed the idea of a double-plume model, where an outer annular plume was always present surrounding an inner axial plume, where gas bubbles remain trapped in the inner plume while water rises in the entrainment region of the outer plume and falls in the detrainment zone. McDougall further suggested that the model can be applied to model an oilwell blowout and predicted that oil would trap in the intrusion layers.

In recent years a series of numerical and experimental efforts were conducted to explore the field of oilwell blowout more extensively. Experimentally, a Joint Industry Project named "Project Deep Spill" was conducted in June 2000, comprising 23 oil companies and the Minerals Management Service in the Helland Hansen region of the Norwegian Sea (Johansen et al. [26]). It was the first large scale intentional deepwater oil spill, in order to study how crude oil behaved when released in deepwater. The trial made several releases of varying combinations of crude oil (750 barrels), marine diesel, methane (18 cubic metres) and nitrogen gas from the seabed at 840 metres below sea-level. Experimental results concluded that during steady releases significant

amounts of oil surfaced in about half the time predicted by their droplet rise velocities. Researchers proposed that the separation of phases due to crossflow current, the effect of the ambient density gradient on the motion of the oil droplets and gas bubbles, and adhesion and other interactions between the different oil phases are all possible phenomena that explains the fate of oil.

Numerically, Zheung & Yapa [56] developed a rigorous model to simulate the behavior of oil and gas accidentally released from deep water. The model formulation integrates hydrodynamics and thermodynamics of the jet and plume, the thermodynamics and kinetics of hydrate formation and decomposition, and gas dissolution. It also has the capability to simulate the behavior of oil and gas in strong cross flow conditions where gases may separate from the main plume. Simulated results were compared with large scale field experiments "Project Deep spill" and verified the model's accuracy (Chen & Yapa [8]).

A recent example of a deep water blowout is the BP Deepwater Horizon oil spill in the Gulf of Mexico in 2010. The tragedy released an estimate of 4.9 million barrels of crude oil into the environment causing ecological, economical and health damage (Frias-Torres & Bostater [17], Horel et al. [24], Lin & Mendelssohn [32]). During the attempt by BP to treat the oil spill, dispersants were used both at the surface and sub-surface to reduce the amount of oil that reached the surface (Lessard & DeMarco [31]). Dispersants were injected at the wellhead of the site for maximum effect. This was the first time in oil spill history that sub-surface dispersant injection was tried and there are conflicting views on its success or failure (Kujawinski et al. [29]). More studies on the effect of dispersants on mitigating oil spills by allowing oil particles to spread in sub-surface intrusions are required.

1.1.2. Bubble plume reservoir aeration and destratification

Another major application of multi-phase plumes is bubble plumes used for reservoir aeration and destratification purposes. This particular area is well studied for a number of years by numerous researchers. The idea of a bubble plume destratification is to provide a strong upward motion in order to mix the different layers of stratification in a water body, including thermal or density stratification (Asaeda & Imberger [3], Leitch & Baines [30], Milgram [36]). This allows denser layers at the bottom of a body to mix with less dense layers at the top. This serves to

balance oxygen and minerals levels within the body to maintain a habitable environment for different organisms and wildlife. For bubble plume aeration, the air flow rate coming out from the bottom is simply weaker to allow small bubbles to fully dissolve within the water body for maximum oxygen intake. Bubble plume aeration is a practical and efficient way of replenishing oxygen supply in a water body (Wüest et al. [52]). Figure 1.1 shows a schematic of both the destratification and aeration plumes illustrated by Socolofsky [43].

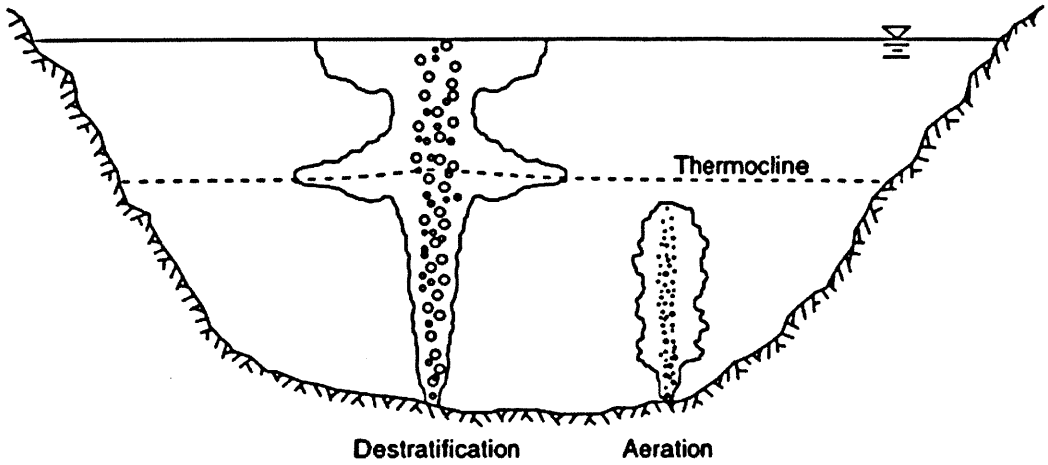

Figure 1-1: Schematic of reservoir bubble plumes for destratification and aeration. (Socolofsky [43])

1.1.3. Carbon dioxide sequestration

Modern society releases a large quantity of greenhouses gases into the atmosphere which has been attributed to industrialization, promoting fossil fuel combustion and deforestation. More than two-thirds of the greenhouses gases are attributed to carbon dioxide CO_2 (Herzog et al. [20]) and such releases are believed to cause adverse effect to the global climate including rise in global temperature (Bolin [5]), extreme weather conditions in regions in the world and increasing chance of natural disasters. In an attempt to moderate climate change, recent studies have explored ways to remove CO_2 from the atmosphere and store it in various places, one of which is the deep ocean.

CO_2 sequestration is the process in which carbons are captured from their sources, isolated and transported, then injected into the ocean. The carbon captured can be of the form of dry ice (Caulfield et al. [7], Nakashiki et al. [37]), $CaCO_3$ mixtures (Rau & Caldeira [38]), dense CO_2

brine solution (Adams et al. [1], Haugen & Drange [19], Sato et al. [40]) or hydrate particles (Holder et al. [22], Warzinski et al. [51]). The preferred forms of storage are mostly negatively buoyant so the CO_2 can sink into the ocean.

Research on CO_2 sequestration has picked up in recent years. Most researchers attempted to quantify the effectiveness of sequestration by numerical methods such as modeling. Integral models were developed by Liro et al. [33] and later modified by Caulfield et al. [7]. Liro et al. [33] took into account the dissolution effects and possible multiple peeling events but neglected density feedback of dissolution. Caulfield et al. [7] improved the model to include density feedback of dissolution and further incorporated a random walk model the time history of pH changes as CO_2 dissolves in the surrounding. Alendal and Drange [2] also completed a two-phase, near-field modeling on releasing CO_2 in the ocean.

However, CO_2 sequestration also presents ecological concerns as dissolving CO_2 lowers the pH of the surrounding waters (Auerbach et al. [4], Caulfield et al. [7], Knutzen [27]). Further understanding plume structure and particle spread will provide addition reference on the effectiveness of such methods.

1.1.4. Sediment laden plume

In addition to the previous applications, the study of multi-phase plumes can be related to aquatic particle laden plumes. These plume applications include transport of silt and soil in rivers and estuaries, dredging and marine waste water disposal, and various geophysical applications such as volcanic or hydrothermal plumes. The study of sediment deposition due to volcanic eruptions is an important field including complex topics such as aircraft safety, climate change, volcanic hazards mitigation, global chemical cycles, and speciation in the deep ocean (Dobran [14], Sparks et al. [42]). A study of multiphase flow is useful in predicting the motions of umbrella clouds in an event of volcanic eruptions, providing an example of a plume trapping in stratification while containing particles. Another example is pyroclastic flows caused by the heated air from the lava flow travelling down the slope of a volcano; they are also buoyancy sources and resemble a multi-phase plume with dense particles.

For underwater applications, hydrothermal plumes caused by volcanic activities are sediment plumes due to precipitation of minerals in the cooler environment of the sea bed. Due to the high

temperature of the discharged fluid at the hydrothermal vents, the resulting flows are highly buoyant. The high temperatures also enable many chemical reactions to occur with the surrounding basaltic rock, releasing Ca, K Si and S ions which are important agents in ocean geochemical exchange and many deep-sea chemosynthetic organisms. Smoker plumes found shallow ocean ridges can also contain gases such as methane and CO_2, forming bubble plumes.

1.2. Thesis organization

This thesis is presented in five chapters. The first chapter presented background related to the applications of multi-phase plumes, especially for deepsea oil spill. The second chapter then goes into the physics of multi-phase plumes and the classification used to identify different plume behaviors. The third chapter then describes the current experimental setup followed by the next chapter which presents our experiments results and findings. The final chapter then discusses the conclusions from the experiments and proposes future work in this area.

2. Multi-phase Plumes

Multi-phase plumes are buoyancy driven flows where the buoyancy is provided by continuous release of an immiscible dispersed phase, such as gas bubbles, liquid droplets or solid particles. The motion of a pure plume is solely buoyancy-driven, as opposed to a pure jet whose motion is driven by its initial momentum. Buoyant jets, or forced plumes, are flows combining initial buoyancy and momentum. A well-studied flow is the single-phase plume, where the released liquid is the same fluid as the surroundings, but is made buoyant by temperature (thermal plumes) or the presence of density-altering solutes such as salt (salinity plumes). The main applications of a single phase plume are sewage, thermal or brine discharges.

2.1. Single Phase Plumes

2.1.1. Governing Equations

The time averaged governing equations for a single phase, buoyant axisymmetric plume are presented below (Chen and Rodi [8], McDougall [35]). Boundary layer approximations were applied stating that the radial derivative of a quantity is much greater than the longitudinal derivative, which is valid far from the source point.

Continuity:

$$\frac{\partial(\rho w r)}{\partial z} + \frac{\partial(\rho v r)}{\partial r} = 0 \tag{2.1}$$

Conservation of momentum in the longitudinal direction:

$$\frac{\partial(\rho w^2 r)}{\partial z} + \frac{\partial(\rho w v r)}{\partial r} = g(\rho - \rho_a)r - \frac{\partial(\rho \overline{w'v'} r)}{\partial r} \tag{2.2}$$

Conservation of mass (concentration):

$$\frac{\partial(\rho w c r)}{\partial z} + \frac{\partial(\rho v c r)}{\partial r} = -\frac{\partial(\rho \overline{v'c'} r)}{\partial r} \tag{2.3}$$

w, v denote the mean local longitudinal and radial velocities, and c represents the mean local concentration of dissolved material.

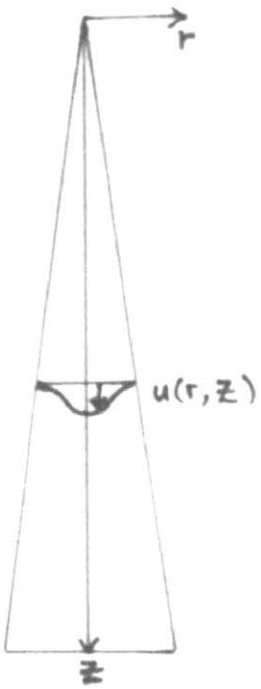

Figure 2-1: Schematic of vertical, single phase and negatively buoyant plume with coordinate system and the radial velocity profile.

The overbars are time averaged values and primed values represent the fluctuations of the value from the mean. ρ_a represents the local ambient density. The gravitational term g is positive for negatively buoyant (sinking) plumes, and negative for a positively buoyant (rising) plume. The gravity vector points in the same direction as the plume.

2.1.2. Integral Method

One of the most effectively ways in dealing with multi-phase plumes is the integral method, or the flux model. To achieve the integral equations, Equations 2.1 to 2.3 are integrated over the entire plume cross-section. Chen and Rodi [8] detail the conversion between the differential governing equations into integral equations. The reason for adapting the integral equations is that they offers a more physically intuitive way of viewing plume dynamics, while retaining quantities of interest such as the volume flux and the buoyancy flux.

The following quantities are of particular interests for multi-phase plumes: volume flux Q, kinematic momentum flux M, and kinematic buoyancy flux $B = gQ(\rho_a - \rho)/\rho_0$. The

kinematic buoyancy can also be viewed as the resultant effect of the weight of the fluid and the surrounding hydrostatic pressure. The definitions are given below:

volume flux Q,

$$Q = \int_0^\infty 2\pi r u dr \tag{2.4}$$

kinematic momentum flux M,

$$M = \int_0^\infty 2\pi r u^2 dr \tag{2.5}$$

kinematic buoyancy flux B,

$$B = \int_0^\infty 2\pi r g' u dr \tag{2.6}$$

where

$$g' = \frac{(\rho_a - \rho)}{\rho_0} g \tag{2.7}$$

with ρ_0 being the density of the ambient at the source point and ρ_a the local ambient density.

Note that in deriving the kinematic fluxes the Boussinesq approximation has been used, and the density is kept constant except in the buoyancy terms. The equations are therefore divided by ρ_0, the density of the ambient at the source point.

Conservation equations for vertical plumes are therefore derived as follow:

Continuity (mass):

$$\frac{dQ}{dz} = 2\pi b(z)|v_e| = 2\pi b(z)\alpha u|_{r=0} \tag{2.8}$$

Momentum:

$$\frac{dM}{dz} = \int_0^\infty 2\pi r g' dr \tag{2.9}$$

Buoyancy:

$$\frac{dB}{dz} = -N^2(z)\int_0^\infty 2\pi r u dr \tag{2.10}$$

where N is the buoyancy frequency, or the Brunt-V¨ais¨al¨a frequency, which is given by:

$$N = \left|\frac{g\partial p}{\rho \partial z}\right|^{1/2} \tag{2.11}$$

The increase of volume flux with height is the integrated entrainment flux $|v_e|$. The constant of proportionality is α, the entrainment coefficient, which is of order 0.1 from previous experiments.

2.1.3. Similarity Solution

To evaluate the integrals in Equations 2.8 to 2.10, it is necessary to assume a velocity and concentration profile at each cross section of the plume.

Mathematically, a similarity solution is used in fluid mechanics to reduce the system of partial differential equations into a simpler ordinary differential equation by combining two or more different physical variables into a new parameter. The solutions were justified as these physical variables are often related to each other in the flow. Derivations by non-dimensionalizing the differential governing equations are carried out by Chen and Rodi [8] in details.

For any z, the local mean velocity can be described by:

$$\frac{u(z)}{u|_{r=0}} = f\left(\frac{r}{b(z)}\right) \tag{2.12}$$

Alternatively, for the one the following quantities j in a model: velocity, concentration or temperature (Kobus [28]):

$$\frac{j(z)}{j|_{r=0}} = g\left(\frac{r}{b(z)}\right) = exp\left(-\frac{r^2}{\lambda b^2}\right) \tag{2.13}$$

where λ, of order 1, differs slightly depending on the quantity represented by j.

For mathematical simplicity, a top hat model is often adopted so that the mean velocity across a plume cross section is assumed constant throughout the section. A Gaussian profile is frequently selected as well.

Physically, the similarity solution means that the shape of the plume cross section profile does not change even as the width of the plume increases as distance increases from the source. It also means that the mean velocity of any point on the plume can be expressed in terms of only the vertical distance from the source and the radial distance away from the plume centerline. This is also called a self-similar, or a self-preserving flow.

Chen and Rodi [8] point out that the buoyancy flux is constant only if the ambient density ρ_a is constant throughout. When such is the case, the integral conservation equations 2.8 to 2.10 can be solved readily to give analytical solutions for the mean flow quantities. However, when ρ_a is not constant such as in a stratified environment, the above governing equations need to be solved numerically as an initial value problem instead.

2.1.4. Plume trapping

Another phenomenon observed for a plume in a stratified environment is plume trapping. This happens when the plume fluid reaches a vertical extent where it becomes neutrally buoyant with respect to its surroundings. At this point the plume fluid will experience a momentum overshoot in which the fluid travels slightly beyond the neutral buoyancy point with momentum acquired from its buoyancy. The plume fluid then no longer travels along the axial direction, but will start to intrude horizontally and spread at the neutrally buoyant height. Turner [50] predicted the trapping height h_t in terms of the initial buoyancy flux B at the source and the buoyancy frequency N of the ambient using dimensional analysis and empirical observations:

$$h_t = 2.8\left(\frac{B}{N^3}\right)^{1/4} \tag{2.14}$$

The plume behavior at the intrusion implies the following: 1) governing equations with the boundary layer approximation no longer hold; 2) the flow is no longer self-similar in the axial direction; and 3) the entrainment coefficient is not constant, and indeed breaks down when the plume no longer moves forward. Other methods of solution exist, including: i) direct numerical simulation (Sato et al. [40]); ii) dimensional analysis; or iii) by returning to the differential equations relaxing several assumptions.

2.2. Double Phase Plumes

2.2.1. Governing integral equations

Double phase or multiphase plumes are buoyant flows where the source of buoyancy is of a different phase than the ambient fluid. These plumes are described in Chapter 1, including oil, bubble and sediment plumes. Figure 2-2 is a schematic comparing the single phase plume to a multi-phase plume. The flow in a multi-phase plume is divided between the dispersed phase (the initial source of buoyancy) and the continuous phase (formed by the ambient fluid).

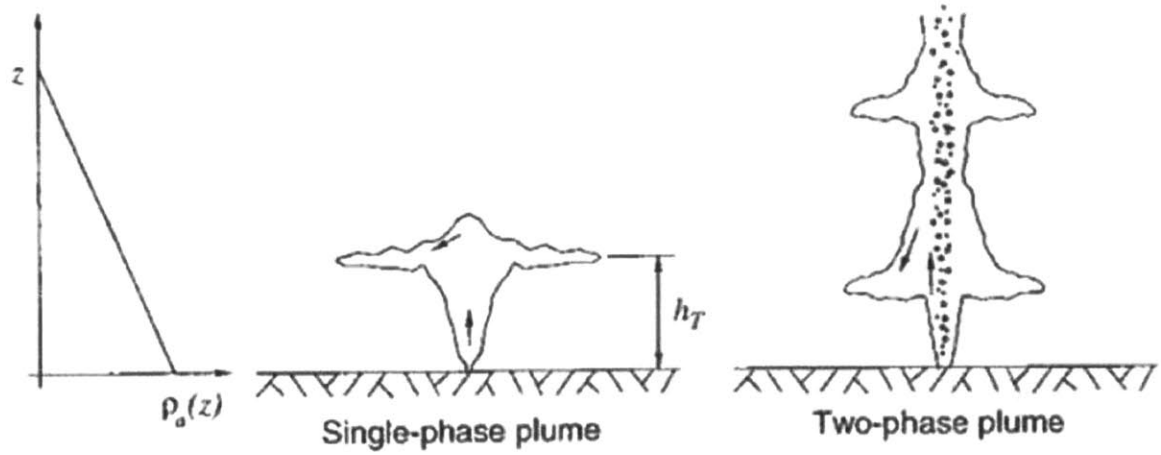

Figure 2-2: Single and bubble plumes in stratification (Socolofsky [43])

The governing equations are similar to those of a single phase plume, except that for multi-phase plumes they need to address both the plume fluid phase and the dispersed phase.

The plume fluid flux Q_p is expressed as:

$$Q_p(z) = \int_0^\infty 2\pi r(1 - C(r,z))\, dr \tag{2.15}$$

where $C(r,z)$ is the particle volume fraction depending on radial distance r and depth z.

The dispersed phase typically travels faster than the plume fluid by a slip velocity u_s, such that the mean transport velocity of the bubbles is $u_b = u + u_s$ (Kobus [28], McDougall [35]). Thus the dispersed phase flux Q_b is:

$$Q_b(z) = \int_0^\infty 2\pi r C(r,z)(u(r,z) + u_s(r,z))\, dr \tag{2.16}$$

The total kinematic momentum flux is the sum of the momentum fluxes of the two phases:

$$\begin{aligned} M(z) &= M_p(z) + M_b(z) \\ &= \gamma \int_0^\infty 2\pi r [u^2(r,z)C(r,z)\big(1 - C(r,z)\big) \\ &\qquad + \frac{\rho_b}{\rho_w}(u(r,z) + u_s(r,z))^2]\, dr \end{aligned} \tag{2.17}$$

where γ is a momentum amplification factor introduced by Milgram [36] that takes into account the additional momentum transport due to turbulent fluctuations from the mean velocity u.

The total kinematic buoyancy flux B of a buoyant release of dispersed phase and continuous phase, in which both phases are buoyant with respect to the local ambient is:

$$\begin{aligned} B(z) &= B_p(z) + B_b(z) \\ &= \int_0^\infty 2\pi r \left[u(r,z) g \frac{\Delta\rho_w(z)}{\rho_w}\big(1 - C(r,z)\big) dr\right] \\ &\qquad + \int_0^\infty 2\pi r [(u(r,z) + u_s(r,z)) g \frac{\Delta\rho_b(z)}{\rho_b} C(r,z)]\, dr \end{aligned} \tag{2.18}$$

Although Equation 2.18 suggests that the buoyancy of the dispersed phase and the continuous dense phase are linearly additive, there may be interaction between the two buoyant phases, like the momentum amplification factor suggested by Milgram [36] for momentum. In a more complex multi-phase plume, there is no clear interaction between the three fluxes of buoyancy, momentum and mass. The dispersed phase interfaces will create additional shear within the interstitial fluid. Additional processes such as the volume expansion of bubbles during its rise, may also affect the overall plume dynamics (McDougall [35]).

2.2.2. Similarity Solution

Consequently, the similarity solution does not necessarily hold true for the double or multi-phase plume. However, in certain literature the velocity, bubble void fraction and concentration profiles are still modeled as a Gaussian profile of the two separate phases like a single phase

plume (Kobus [28], McDougall [35], Milgram [36]). Equation 2.13 is used with various values for constant λ for each of the two phases in similarity solutions. This assumption is supported by experimental observations of bubble plumes in unstratified environments (Kobus [28]), and also in gas bubble jets in various liquid or gas systems (Tacke et al. [47]). In other literature, the plume release has been modeled as a double plume, made up of an inner core, containing the dispersed phase, with an outer plume region that is free of bubbles or droplets (Asaeda & Imberger [3], Crounse et al. [12], McDougall [35]).

2.2.3. Plume Trapping and Peeling

In a stratified environment for multiphase plumes another phenomenon is also observed: plume peeling. This occurs due to the dispersed phase particles or droplets, being unable to mix locally with the entrained fluid, will always remain buoyant, while the continuous phase is able to dilute and often reverse buoyancy. This results in that the plume fluid 'peels' and leaves the dispersed phase at a level near its neutral buoyancy. The depth or height at which this occurs is called the peeling depth or height. Socolofsky [44] predicts the fraction of fluid that leaves the plume core in the first peeling event, as a function of initial plume release conditions as detailed in the next Section 2.2.4.

2.2.4. Plume behavior and structure

Past investigations on plume structure mainly pertain to optimizing reservoir destratification. Asaeda and Imberger [3] classified plumes as exhibiting three distinct behaviors, or types. Type 1 plumes have no intermediate intrusion layers, except when they impinge on a surface. Type 2 plumes have one or more distinct intrusions, and Type 3 plumes show continuous peeling from the plume core, resulting in a random set of intrusions.

Experiments by Socolofsky and Adams [45] also identified a new type, Type 1*, slightly different from Type 2 in which bubbles are carried into the intrusion layers temporarily. All four types of plume behavior are illustrated in Figure 2-3. Socolofsky and Adams [45] introduced a parameter, the non-dimensional slip velocity U_N, to relate the observed plume type with only the plume source and ambient conditions.

U_N is defined by:

$$U_N = \frac{u_s}{(BN)^{1/4}} \tag{2.19}$$

where u_s is the slip velocity of the dispersed phase droplets or particles, B the initial kinematic buoyancy flux, and N the Brunt-V¨ais¨al¨a frequency, or stratification frequency of the ambient.

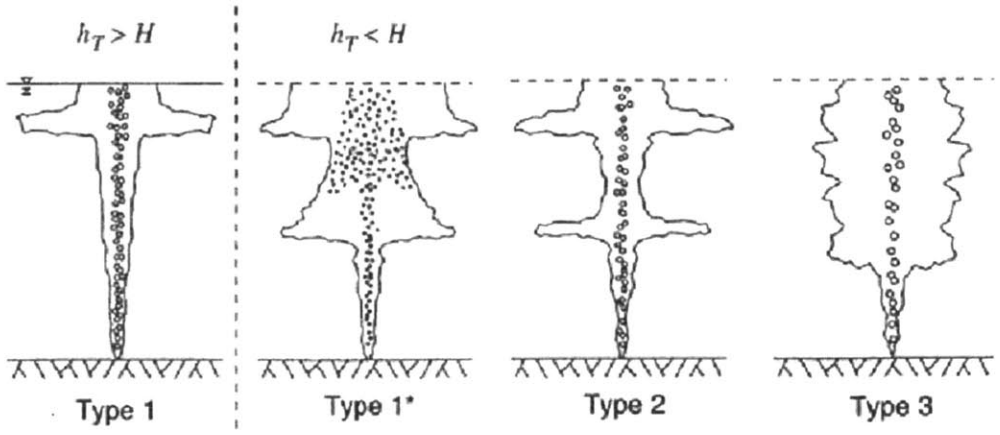

Figure 2-3: Stagnant multi-phase plume structures (Socolofsky and Adams [45])

The denominator, $(BN)^{1/4}$, is a characteristic plume fluid velocity. They found that Type 1* plume behavior is observed for $U_N < 1.4$, Type 2 for $1.4 < U_N < 2.4$, and Type 3 for $U_N > 2.4$.

In the current work, the observed plume type will cover a spectrum of U_N ranging from 0.07 to 1.5. This include plume structure mostly in Type 1* and some in Type 2. Experimental results suggested that the typology introduced by Socolofsky and Adams [45] can be expanded further to provide a better description of the plume structure (Figure 4-5), and the modification of the typology will be discussed in Section 4.3.

2.2.5. Prediction of Particle Spread

One of the most important behaviors exhibited by a multi-phase plume is its radial particle spread due to outward advection by the plume intrusion layer. The following section discuss one of most common and theoretically sound ways of predicting radial spread for fine particles.

The following model is presented by Chow [10], and is based on an estimation of the settling particles' residence time within the intrusion layer, and is applicable only to fine particles with

U_N value much less than one. Consider the plume fluid in the intrusion layer of a Type 1* plume. Upon vertically overshooting the neutrally buoyant level, its turbulent kinetic energy will transfer into buoyant potential energy. While the vertical momentum of the plume will drop to zero at the peel height, there is a local lateral density gradient which translates to a pressure gradient, resulting in lateral intrusion. Cardoso and Woods [6] suggest that, since the intrusions have a sharp leading edge, and a smooth outer appearance compared to the plume itself, there is lower turbulence in the intrusion layer. In addition, continuity and axisymmetry dictates an intrusion layer to form. As the intrusion layer spreads radially outward, the sediment particles will begin to settle out of the intrusion layer by their own weight.

Let the particles fall at their slip velocity u_s through the intrusion layer, and a constant thickness of the intrusion layer Δh (Figure 2-4) (Chow [10]). In an axisymmetric intrusion, the intrusion is modeled as a cylinder whose radius increases with time. It is observed in experiments that particles leaving the intrusion layer will fall passively to the bottom of the tank, meaning that there exists a radial spread within the intrusion layer. Therefore the residence time of particles in the intrusion layer will determine the bottom sediment radial spread.

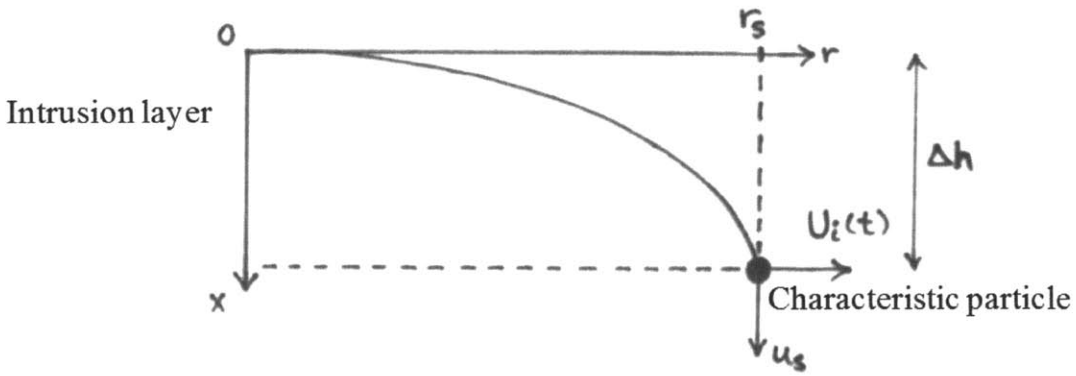

Figure 2-4: Characteristic particle trajectory through plume intrusion layer (Chow [10])

Well-Mixed Model

In the current experiment, the radial particle spread can be modeled as a well-mixed model. As suggested by Chow [10], if the particles are well mixed in the intrusion layer, the governing equation for the concentration of sediment in the layer C is given by:

$$\frac{dC}{dt} = -\frac{u_s}{\Delta h}C \tag{2.20}$$

yielding the time evolution of concentration of sediment in the intrusion layer:

$$C = C_0 \exp\left(-\frac{u_s}{\Delta h}t\right) \tag{2.21}$$

where C_0 is the mean concentration of sediment entering the intrusion layer. The time can be translated into the radial distance by

$$Q_i t = \pi r^2 \Delta h \tag{2.22}$$

Substituting the expression for t from Equation 2.22 into Equation 2.21 gives

$$C = C_0 \exp\left(-\frac{r^2 \pi u_s}{Q_i}\right) = C_0 \exp\left(-\frac{r^2}{\sigma_r^2}\right) \tag{2.23}$$

where

$$\sigma_r = \sqrt{\frac{Q_i}{\pi u_s}} \tag{2.24}$$

Q_i is obtained from Socolofsky and Adams [43]:

$$\frac{Q_i}{(B^3/N^5)^{1/4}} = 0.9 - 0.38\left(\frac{u_s}{(BN)^{\frac{1}{4}}}\right)^{0.24} \tag{2.25}$$

thus yielding the following relationship:

$$\sigma_r = \sqrt{\frac{0.9 - 0.38(U_N)^{0.24}}{\pi}} \frac{B^{3/8}}{N^{5/8} u_s^{1/2}} \tag{2.26}$$

Note that $\sigma_r = r_s$, and Equation 2.23 describes a radial Gaussian distribution for the sediment concentration below the intrusion layer.

Figure 2-5 demonstrates the prediction for modeling sedimentation for fine sediment out of the plume intrusion layer.

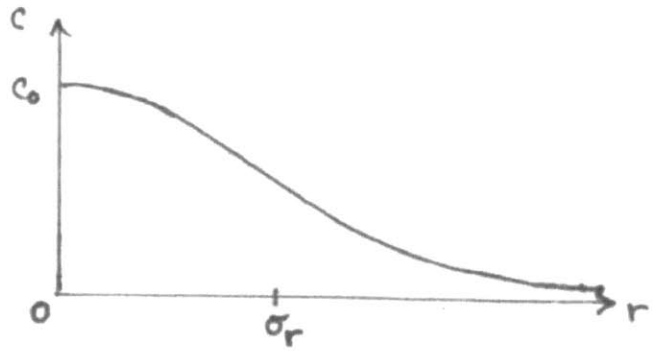

Figure 2-5: Well-mixed model illustrated by a Gaussian profile with standard deviation $\boldsymbol{\sigma_r}$

Kurtosis

To verify that our distribution resembles a Gaussian distribution, the kurtosis of each distribution was calculated and compared to that of a standard Gaussian distribution. By definition in probability theory and statistics, kurtosis α_4 measure the 'peakedness' of a distribution and is a descriptor of the shape.

$$\alpha_4 = \frac{\mu_4}{\mu_2^2} \tag{2.27}$$

where the ith-moment μ_i of a distribution is

$$\mu_i = \int_0^\infty 2\pi r^{i+1}\, dr \tag{2.28}$$

The excess kurtosis of a distribution is

$$K_4 = \alpha_4 - 2 \tag{2.29}$$

Figure 2-6 shows values of kurtosis for other distributions. For a standard Gaussian distribution, the excess kurtosis is 0 (black line in Figure 2-6).

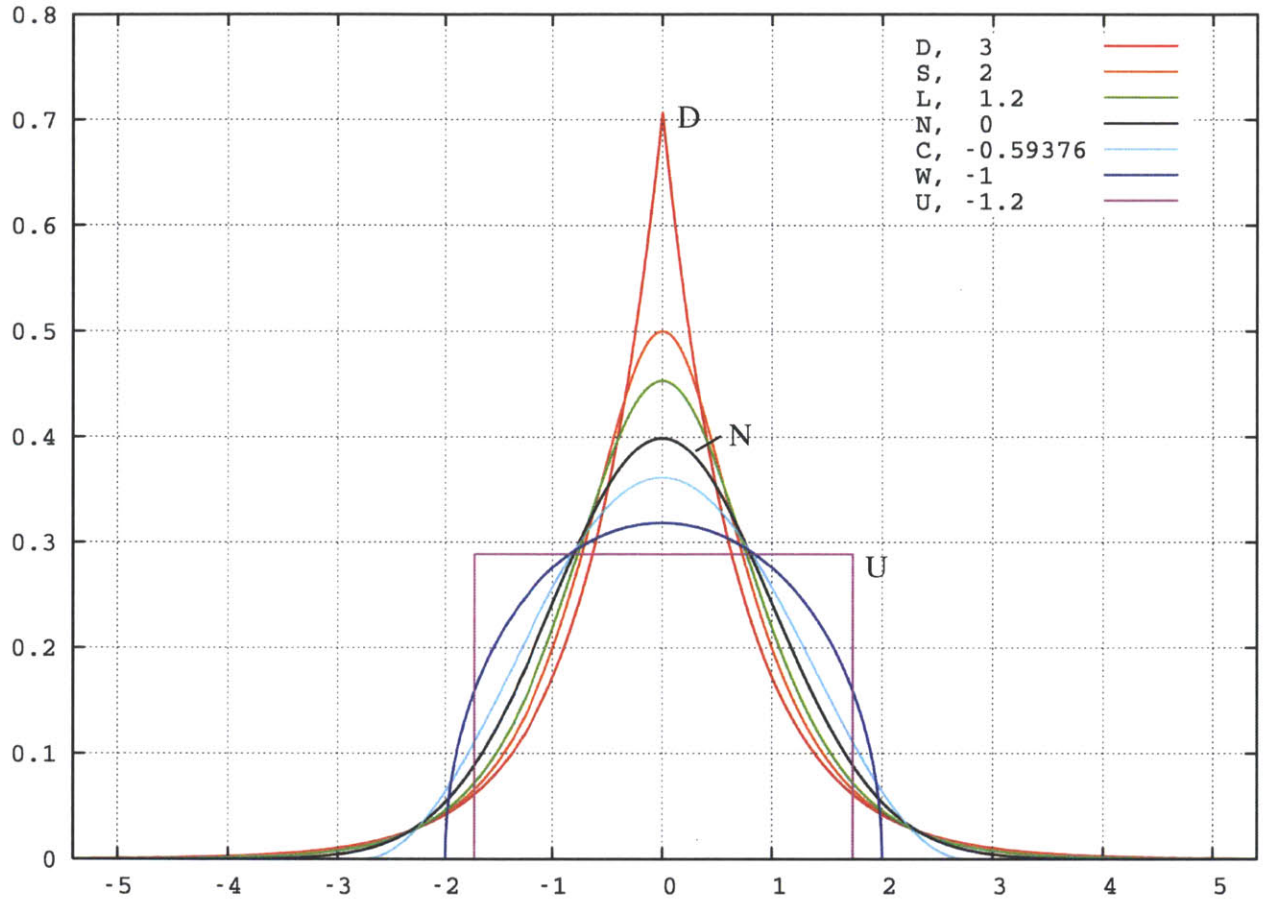

Figure 2-6: Shape and kurtosis of different common distributions.
(N = 0 denote a Gaussian profile) (Wikimedia Commons, retrieved online October 2, 2012)

2.3. Focus of Current Work

The current experiments will focus on stable linear stratification with no crossflow current. Both the dispersed phase will be negatively buoyant with respect to the ambient. This is to model the behavior of a scenario of a sub-surface oil spill, in which oil and gas droplets of different size emerges from the ocean floor and travel through a deep water column. The main experimental data, the dispersed phase radial spread will be observed for Type 1* and 2 plumes (Details explained in Chapter 4.3).

In the current experiments, the oil droplets are modeled by different size of glass beads with the same density. The typical values of U_N of the plume release are from 0.07 to 1.5. They are expected to have mainly Type 1* behaviors.

3. Experimental Setup

This chapter describes the methods and equipments used for the experiments conducted in the current thesis. Previous researchers including Socolofsky [43], Ruggaber [39] and Chow [10] in the Parsons Lab at MIT carried out experiments on plume dynamics in stagnant stratification with much of the same apparatus. The current system largely follows the experimental setup described by Chow [10], with slight adjustment and new parts introduced according to the need of the current experiments. If further explanation is required please refer to Socolofsky [43] for a more thorough description. The current setup employs the following equipments and methods:

- The tall experimental tank
- Two-tank stratification method
- Density meter
- Buoyancy sources (glass beads)
- Collection trays to determine particle spread
- Sieves for particles separation (only for experiments with beads of different sizes)

3.1. Experimental Tank

The main apparatus for the experiments is a tall experimental tank located at the Parsons Laboratory for Environmental Science and Engineering at MIT. The tank was built specifically for a salinity-stratified environment, and it measures 1.22 m square by 2.44 m tall and was built by Excalibur Glassworks, Inc. of Woburn, Massachusetts in June 1997. It was made with 38mm thick, two-ply, fully tempered laminated glass. Figure 3-1 shows a schematic of the tank and its dimensions.

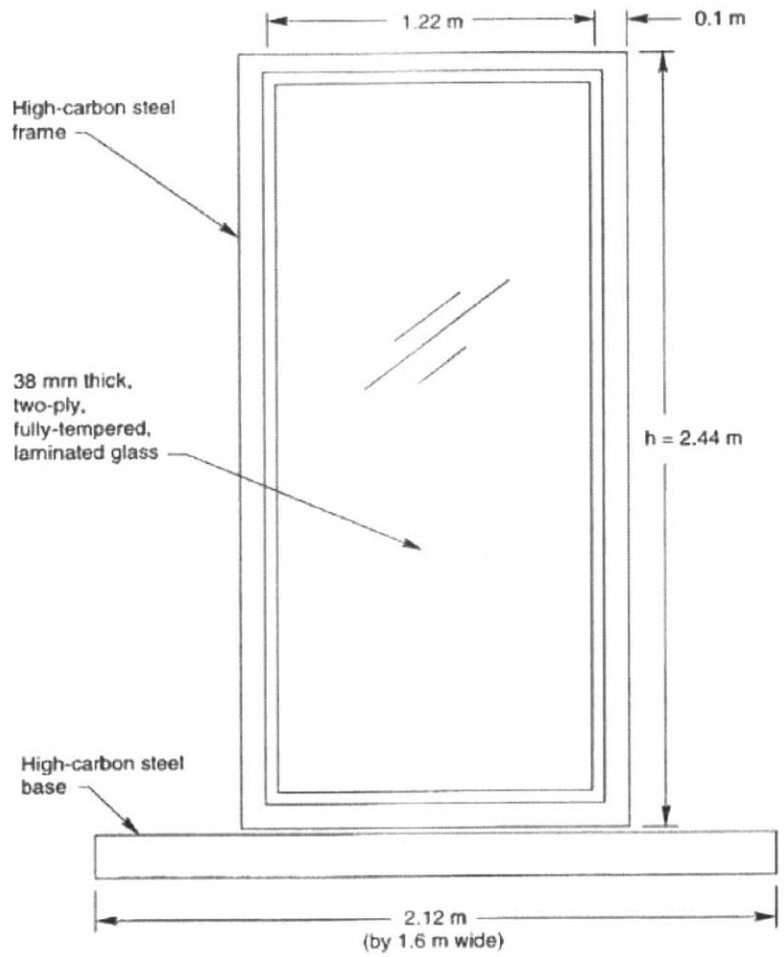

Figure 3-1: Dimension of the experimental tank (from Socolofsky [43])

The first peel height of a typical bubble flow used by Socolofsky [43] in the design of the tank was about 1.2 m above the release point with a maximum U_N of 1.5, well within the maximum depth of 2.4 m. Socolofsky observed at least two discrete, Type 2 peels, without technical difficulties and the current experiments were expected to do the same. The current experiments were negatively buoyant with U_N ranging from 0.07 to 1.5, and are expected to exhibit only one visible peel and intrusion layer. As a result, the depth of the tank was more than sufficient to observe the peeling and trapping depths of the negatively buoyant plumes. In addition, the remainder of the depth was traversed by the sediment particles which fell out of the intrusion layer after radial spread, and their post-peel behavior was able to be observed. For a long enough experimental time, the plume intrusion layers are expected to contact the tank walls.

According to Socolofsky [43], if the volume of the intrusion layer V_i when contacting the tank is modeled as a cylinder with the same diameter as the tank width w, and with a uniform thickness of half the difference of trap and peel height, i.e.,

$$V_i = \frac{1}{2}(h_p - h_t)\frac{1}{4}\pi\omega^2 \tag{3.1}$$

then an estimated time for contact to occur could be given by dividing a predicted intrusion layer volume, V_i by an estimate of the intrusion flux, Q_i based on plume and stratification conditions (Equation 2.24 from Socolofsky [43]):

$$t \sim \frac{V_i}{Q_i} = \frac{\frac{1}{2}(h_p - h_t)\frac{1}{4}\pi\omega^2}{0.9(B^3/N^5)^{1/4}} \tag{3.2}$$

where w = 1.2m. The predicted times for the different experimental runs were about four times greater than the planned duration of the experiments. In the current experiments, fine sediment spread radially and in general less than 5% of the sediment made its way out to the furthest collecting cells. As the particles were released in the center of the tank, the plume dynamics was largely unaffected by the sides. In addition, the plume intrusions were observed to travel horizontally in the tank away from the centerline during each experiment; therefore the trap and peeling depth should not be affected by the side walls. Based on these calculations, the width of the tank was sufficient for the current experiments to model a laterally infinite domain.

3.2. Stratification

In the current experiments, constant values for N, the Brunt-V¨ais¨al¨a frequency, were obtained by maintaining a linear density gradient over the traveling region of the plume. Achieving constant values of N is essential in our experiment's accuracy because predictions of U_N and sediment spread both depend on N, making it an important parameter to maintain.

3.2.1. Two Tank Method

The tank was stratified using the two-tank method (Hill [21]), which is capable of producing any arbitrary salt density stratification profile, as shown in Figure 3-2. The second tank in the

method's naming refers to the well stirred mixing tank for preparing the local salt for pumping into the main experimental tank. Initially, the mixing tank had a density equal to the maximum desired for the final density profile in the experimental tank. As the main tank was filled from the top, freshwater was added to the mixing tank, the rate of which determined the rate of decrease in density. In addition, to minimize vertical mixing of the lower density layers by the incoming water, a perforated splash plate made of plastic of the size of the cross-section of the tank, topped with horsehair and supported by styrofoam floaters, was used to divert the incoming salt water sideways.

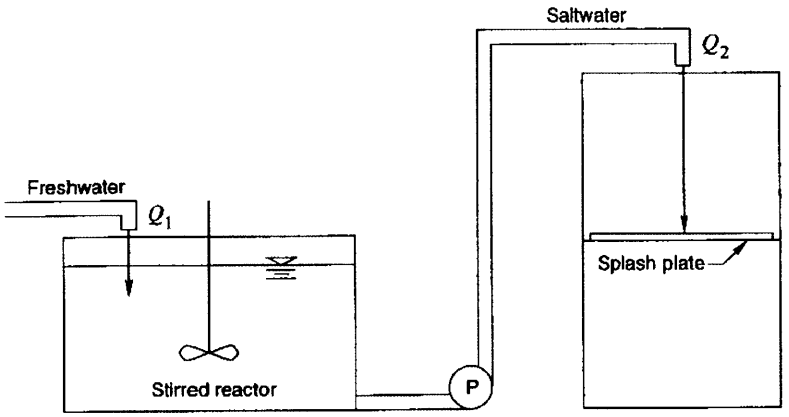

Figure 3-2: Illustration of the two-tank stratification method (from Socolofsky [43])

For a mixing tank which is well mixed, with initial volume V_0 and salt concentration C_0, receiving freshwater at a rate Q_1 and delivering saltwater to the experimental tank at a rate Q_2, the change of salt concentration over time in the water received by the latter C(t), is given by (Hill [21]):

$$\frac{C(t)}{C_0} = \left(\frac{V_0 - (Q_2 - Q_1)t}{V_0}\right)^{\frac{Q_1}{Q_2 - Q_1}} \tag{3.3}$$

To achieve a linear profile, the exponent needs to be 1, requiring $Q_2 = 2Q_1$. In addition, to attain C = 0 at the top of the tank, V_0 needs to be half the volume of the experimental tank.

For the current experiments, the freshwater was fed via a 3.8 cm (1.5 in) local water supply into a 1890 L (500 gallons) tank measuring 61cm (24 in) in diameter and 2m (80 in) deep. To make

up the initial salt solution, 36 kg (80 lb) of salt (Cargill food grade sodium chloride) was placed into the mixing tank, and freshwater was added to the initial water level, to make up a solution of about 1020 kg/m^3. During the stratification process, a boat motor was placed in the tank to encourage continuous mixing. A drain at the bottom of the tank connected a pipe to the experimental tank.

A corrosion-resistant centrifugal pump (Teel model number 4RJ44) was used to deliver the salt solution into the experimental tank. In order to prevent air bubbles from entering the pump, the mixing tank was not allowed to completely empty out. Instead, the mixing tank retained about 10 cm of water depth by the end of the stratification process. One consequence of not emptying the tank was that the surface of the tank did not achieve zero salinity if the water flow rates in and out of the tank were kept constant. But since the experimental predictions and observations only require a smooth density gradient, and since the source for the experiments conducted were placed at least 15cm below the surface, the absolute density at the top of the tank was not important.

The flows of the freshwater and saltwater lines were monitored by passing both lines through identical rotometers, each with a scale of 0.4 to 3.6 l/s (6 to 60 gpm). Ball valves were also placed in the line for manual adjustment of the two flows until the saltwater flow was twice the freshwater flow. In the experiments, typical freshwater Q_1 and saltwater Q_2 flows were 1.77 and 3.54 l/s (28 and 56 gpm) respectively.

3.2.2. Measurement of Density Gradient

The density profile of the stratified tank was measured using an equation of state (McCutcheon et al. [34]):

$$\rho = 1000\left(1 - \frac{(T + 288.9414)}{508929.2(T + 68.12963)}(T - 3.9863)^2\right) + AS + BS^{1.5} + CS^2 \tag{3.4}$$

where T is the temperature in degrees C, S the salinity in g/kg, and

$$A = 0.824493 - 0.0040899T + 0.000076438T^2 - 0.00000082467T^3 + 0.0000000053675T^4$$

$$B = 0.005724 + 0.00010227T - 0.0000016546T^2$$

$$C = 0.00048314$$

The equipment used to measure the density profile was an YSI Model 33 S-C-T (Salinity-Conductivity-Temperature) meter manufactured by YSI incorporated. Salinity measurements were taken every 20 cm from the bottom to the top of the tank to determine the density profile in the experiments. The Brunt-V¨ais¨al¨a frequency N, is then calculated according to the profile recorded in each experiment and the data are reported in Section 4.1. Figure 3-3 shows a typical density profile for the current experiments.

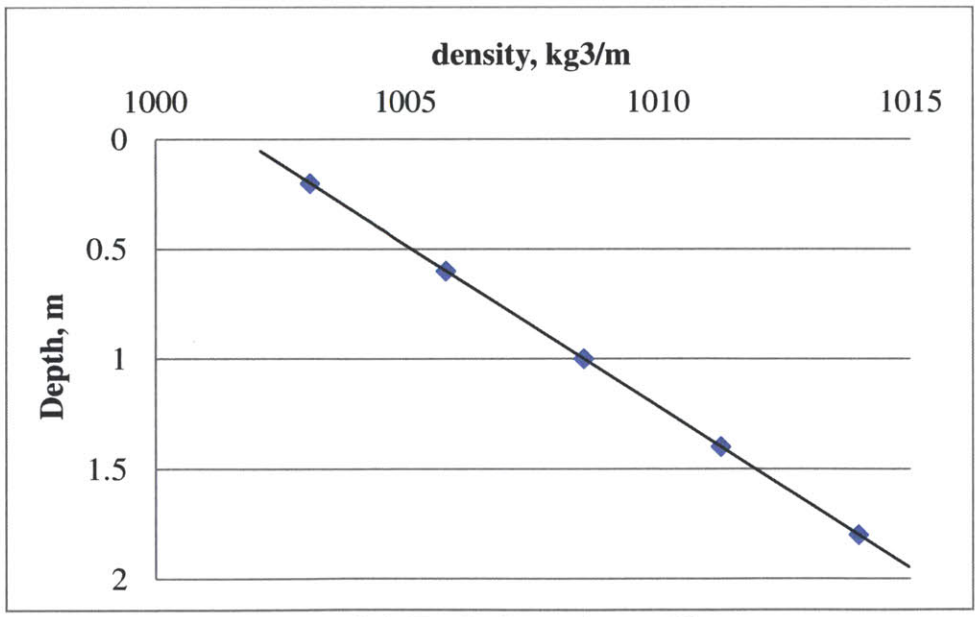

Figure 3-3: Typical Density profile.

3.3. Buoyancy Sources

The driving force for the motion of the multiphase plume is its initial buoyancy flux, B. In the current work, the buoyancy consists only the contribution from the particles, and the definition of initial buoyancy is:

$$B = Qg\frac{\rho_b - \rho_0}{\rho_0} \tag{3.5}$$

where Q is the flow rate of particles, ρ_b density of the particles and ρ_0 density of the ambient.

3.3.1. Glass Beads

The non-dimensional slip velocity $U_N = \frac{u_s}{(BN)^{1/4}}$, where B is the initial buoyancy flux and N the stratification frequency, is highly dependent on the size and the density of the particles used as the buoyancy source. This parameter heavily influences the plume characteristics, structure and particle radial spread.

The current work focused on a range of U_N values between 0.07 and 1.5. This include right different particle sizes and results in a variety of plume structures including Type 1* and 2.

The only materials chosen for the current experiments are silicon glass beads. The glass beads were Ballotini impact glass beads (From Potters Industries, Malvern, PA), used for finishing smooth metal surfaces in industry. Eight size classes provided by the vendor were used, including A, B, C, D, AD, AE, AF, AG and AH. The diameters of the beads are given in Table 3-1 along with their slip velocities.

Bead	Mean Diameter (microns)	u_s (cm/s)
A	725.0	10.907
B	512.5	7.446
C	337.5	4.476
D	256.0	3.103
AD	159.0	1.560
AE	120.0	1.005
AG	89.0	0.614
AH	67.5	0.380

Table 3-1: Table of beads with their slip velocity.

3.3.2. Determination of Slip Velocity

To determine the slip velocity, an empirical relation suggested by Dietrich [13] was used based on the diameters of the particles, assuming spherical particles:

$$\log(W_S^*) = -3.76715 + 1.92944(\log(D^*)) - 0.09815(\log(D^*))^2 - 0.00575(\log(D^*))^3 + 0.00056(\log(D^*))^4 \quad (3.6)$$

where the non-dimensional diameter and terminal velocity are given by

$$D^* = \frac{(\rho_s - \rho)gd^3}{\rho\nu^2}$$

$$W^* = \frac{u_s^3}{(\rho_s - \rho)g\nu}$$

where ρ_s and ρ are the density of the particles and ambient fluid respectively, and ν the kinematic viscosity of the ambient fluid.

3.3.3. Release Mechanism

Figure 3-4 shows a schematic of the glass particle's release method. Glass beads were released from a 1 liter glass bottle by gravity. A 12V vibrator powered by a 3V DC transformer was also placed at the top of the bottle to facilitate steady bead flow. A funnel served to hold experimental glass beads rested on a PVC and bronze pipe setup which spanned across the top of the tank as shown in Figure 3-4.

In order to deliver a steady flow of glass beads, a 20 L (5.3 gal) carboy was modified to become a large Mariotte siphon to provide water to facilitate flow, as described in Fischer et al. [16]. A tube was placed so that it opens to the atmosphere out of the top and penetrates underneath the surface of the water to keep the discharging water at a constant pressure head. As the bottle emptied, a partial vacuum was created in the cavity between the top of the bottle and the water level to keep the pressure head constant.

The conduit in which the glass beads and water met was placed close to the water surface to minimize the initial momentum of the fluid as it discharged into to the experimental tank. The particles were added inline to the flow just prior to the point where the combined flow was diverted downwards into the source release point. Air bubbles that might enter the line were minimized by keeping the conduit running full. This was achieved by placing a small piece of

sponge near the entry funnel of the water to trap small gas bubbles. This semi-permeable sponge also served to reduce the momentum of the discharging fluid into the experimental tank.

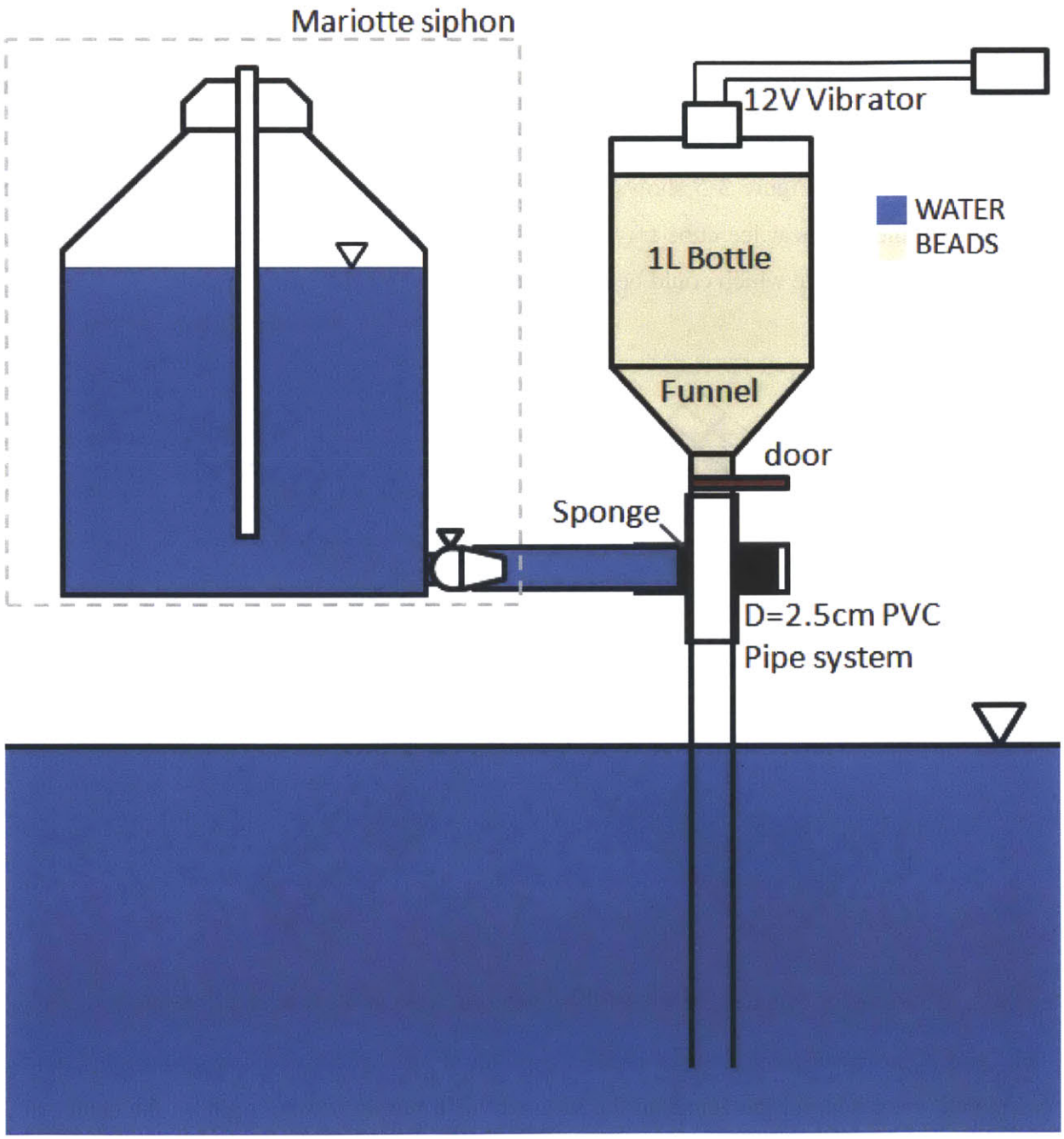

Figure 3-4: Schematic of the glass particles release method.

3.3.4. Determination of Flow Rates

Using the glass delivery method, the two flow rates of water and glass particles could be measured separately. The volume flow rate of the water out of the carboy was measured by timing a known volume. The mass flow of the glass beads was also timed, and was converted via its density to a volumetric flow rate. The flow rates are presented in Table 4-1 in the next chapter.

3.4. Particle Spread

The radial spread of the sediment advected by the plume, was measured by collecting the particles from beneath the peel event, in a series of 126 collecting trays measuring 3.5 cm by 6.0 cm by 3.0 cm deep. Figure 3-5 shows the horizontal arrangement of the collection trays used. They were nine identical ice cube trays arranged in a diagonal cross, centered in the tank, and attached to a rigid plate which could be raised and lowered by pulley in the tank.

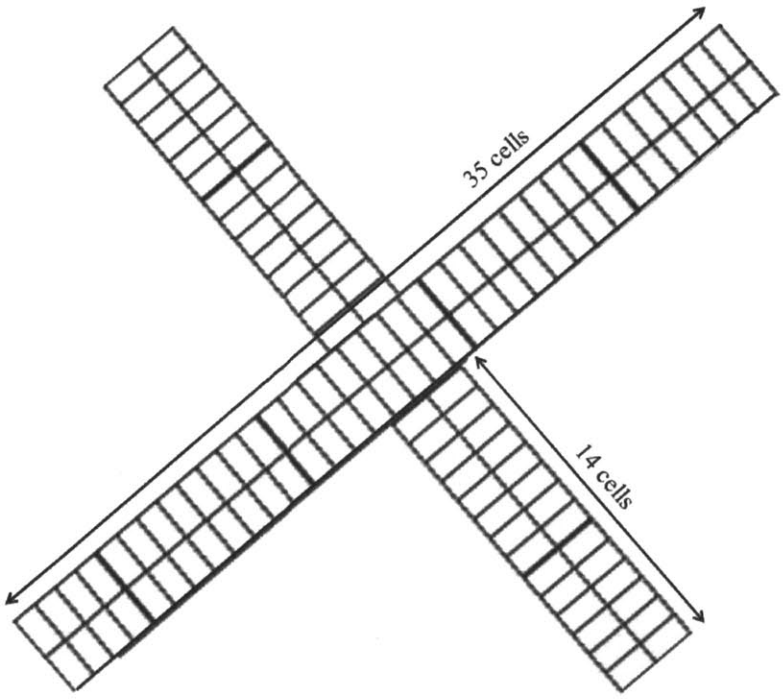

Figure 3-5: Arrangement of the collection trays at the bottom of the tank.

This particular configuration was chosen so that a two dimensional distribution could be calculated, even without the center of the sediment distribution landing right on the center of the cross structure, either because the plume direction was not directed quite vertically, or if any

circulation was created to translate the entire sediment distribution horizontally. However, for most of the experiments the region of the center of the cross arrangement were indeed close (within 10 cm) to the center of the radial sediment distribution. A sample radial spread is shown in Figure 3-6.The sediment collection tray at the bottom of the tank was 195 cm below the plume source.

Chow [10] suggested that if the spread does not change significantly with the distance traversed by the sediment, it can be argued that the sediment particles were simply passively falling in the post-peel stage, as described by a Type 2 plume.

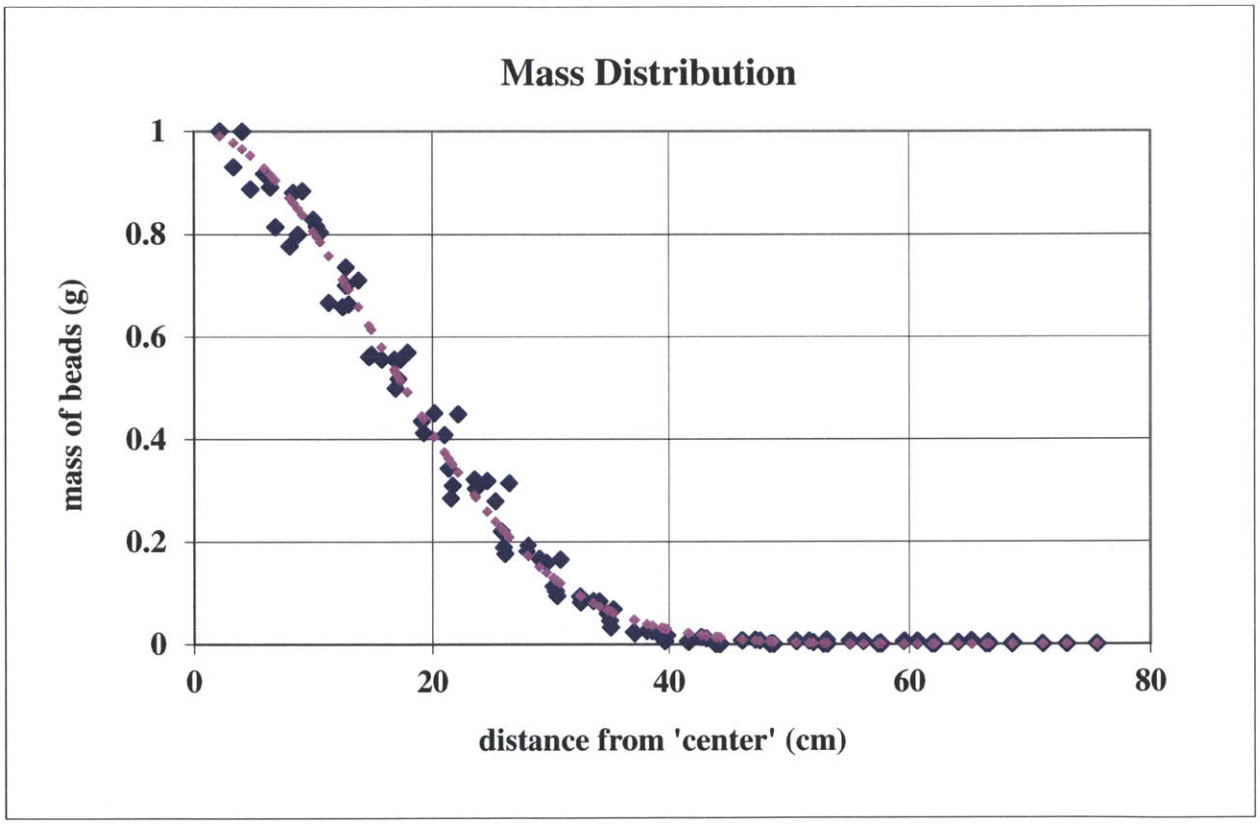

Figure 3-6: Sample radial spread.

After the tank was drained, collected samples were lifted out of the tank by a pulley, and the collected trays were dried under a heat lamp and fan overnight. Particles from each dried individual cell with assigned lateral coordinates were brushed out onto a weighing tray, and weighed on an analytical balance, to provide a lateral mass distribution.

For the experiments with two different bead sizes, sieves were used to separate particles of different sizes in each collected samples before measuring the sample weights. The current experiments utilized a 100μm for experiments between particle size B & D and a 300 μm sieves for experiments between particle size B & AG and size D & AG.

4. Results

4.1. Initial Conditions

This chapter presents the results acquired from the experiments conducted in this thesis and discusses their validity and applications. The initial conditions of the experiments conducted with one single bead size are listed in Table 4-1, including the particle size, particle density, slip velocity and the amount of mass released per experiment. The flow rate Q, buoyancy flux B and stratification frequency N are also calculated to determined the non-dimensional slip velocity U_N for each experiment. A total of twelve experiments including eight different bead sizes were conducted. Experiments with particle size B and AG were performed three times to verify the reliability and accuracy of the current experiments.

Particles	Particles median diameter (μm)	ρ_b (kg/m^3)	u_s (cm/s)	Mass released (kg)	Duration of release (s)	Q_b (m^3/s)	B (m^4/s^3)	N (1/s)	U_N
A	725	2450	10.907	0.75	38	8.06E-06	1.15E-04	0.255	1.483
B (1)	512.5	2450	7.446	1	55	7.42E-06	1.06E-04	0.263	1.025
B (2)	512.5	2450	7.446	1	50	8.16E-06	1.16E-04	0.25	1.014
B (3)	512.5	2450	7.446	1	45	9.07E-06	1.29E-04	0.254	0.984
C	337.5	2450	4.476	1	60	6.80E-06	9.70E-05	0.262	0.630
D	256	2450	3.103	1	69	5.92E-06	8.43E-05	0.251	0.457
AD	159	2450	1.560	1	78	5.23E-06	7.46E-05	0.254	0.236
AE	120	2450	1.005	1	94	4.34E-06	6.19E-05	0.26	0.159
AG (1)	89	2450	0.614	1	135	3.02E-06	4.31E-05	0.258	0.106
AG (2)	89	2450	0.614	1	125	3.27E-06	4.65E-05	0.253	0.105
AG (3)	89	2450	0.614	1	130	3.14E-06	4.48E-05	0.261	0.105
AH	67.5	2450	0.380	1	210	1.94E-06	2.77E-05	0.254	0.074

Table 4-1: Initial conditions for current experiments.

4.2. Radial Sediment Spread for Particles of a Range of Different Sizes

One of the main properties which is of particular significance to the current study is the radial sediment spread for each particle size. The goal is to construct a relationship between particle size and plume radial spread. This was done by relating the non-dimensional slip velocity U_N to the standard deviation of the plume distribution σ_r. The following section discusses the validity of assuming a Gaussian plume spread and the method behind the determination of σ_r for each experimental trial.

4.2.1. Experimental Determination of Data Points

The radial spread of the descending sediment was determined using the mass recorded from the collection trays. Collected samples were dried by heat lamps and fans, and particles from individual cells with assigned coordinates were weighed. After all the cells were weighed, the center of the distribution was determined to be the position that results in the smallest least square value. Since initial observation of the distributions showed that the resulting sediment spread resemble two-dimensional Gaussian distributions, a simple analysis was carried out for each distribution to compare the radial spread with a standard Gaussian distribution. After the analysis, the sediment spread can then be taken as the radial variance of each distribution.

4.2.2. Discussion of distribution

In order to verify the assumption that the distributions are Gaussian, the kurtosis of each experimental distribution was calculated. For a detailed explanation on the kurtosis and their application, please refer to Section 2.2.5. In general, a normal distribution, or a Gaussian distribution, can be characterized by an excess kurtosis K of value zero. Table 4-2 shows the excess kurtosis of the distributions for every experimental trial. The computed kurtosis of all distributions ranges between -0.357 to 0.203, which are close to zero accounting for experimental errors and variations. This suggested that the radial spread of the particle plumes closely resembles a Gaussian distribution.

A Gaussian fit was also plotted with experimental data from each experiment; an example of such plot is shown in Figure 4-1. It was observed that the difference between the Gaussian fit and the experimental data points was minimal. Together with the conclusion drawn from the kurtosis

analysis, the distributions can therefore be assumed Gaussian. The variances and standard deviations can then be obtained for all distributions from the center, and σ_r taken to be the radial sediment spread from the distributions, with values listed in Table 4-2. Details on extracting σ_r from raw experimental data are presented in the next section.

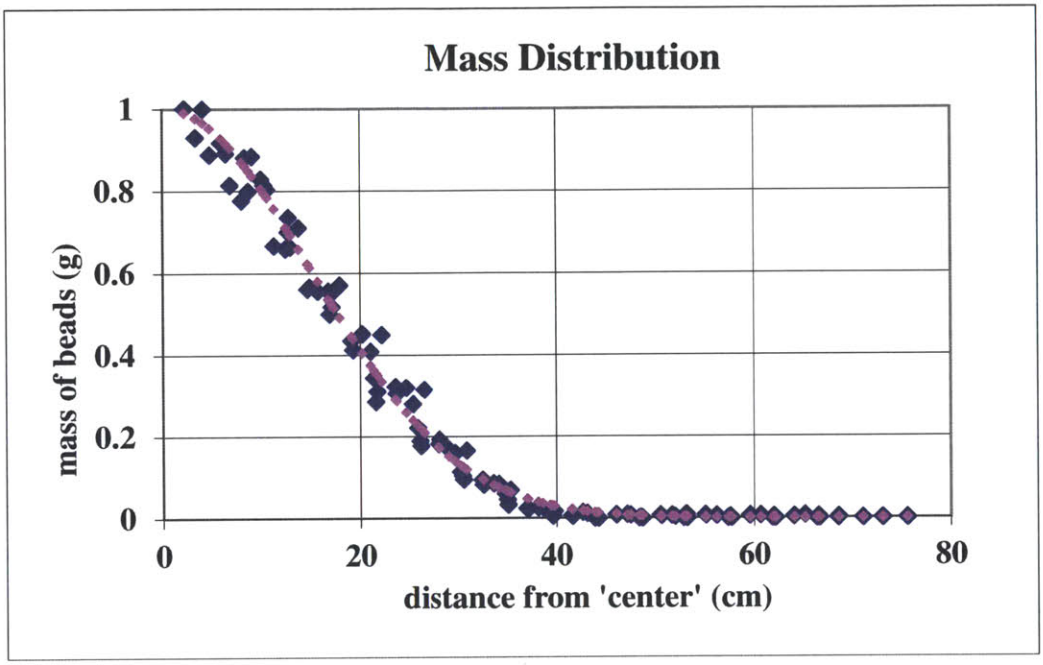

Figure 4-1: A sample of a fit of the 2-D Gaussian distribution.

Particles	U_N	K	σ_r (cm)	σ_r / H	$\overline{\sigma_r}$ (cm)	$\overline{\sigma_r} / H$
A	1.495	0.203	8.2	0.0432	8.2	0.0432
B (1)	1.032	-0.005	8.2	0.0432	9.667	0.0509
B (2)	1.021	-0.101	10.6	0.0558		
B (3)	0.991	0.000	10.2	0.0537		
C	0.606	-0.182	13	0.0684	13	0.0684
D	0.457	-0.280	15	0.0789	15	0.0789
AD	0.212	-0.330	21.3	0.112	21.3	0.112
AE	0.158	-0.235	32.2	0.169	32.2	0.169
AG (1)	0.090	-0.245	34.6	0.182	34.933	0.184
AG (2)	0.0888	-0.188	37.6	0.198		
AG (3)	0.0889	-0.198	32.6	0.172		
AH	0.0738	-0.357	41	0.216	41	0.216

Table 4-2: Results table showing excess kurtosis for every experimental trials and their radial sediment spread.

4.2.3. Determining the Radial Spread

The method of fitting a 2-D Gaussian distribution and computing radial spread is presented as follow:

A two-dimensional Gaussian distribution describing the concentration $c(r)$ of sediment, with maximum and mean located at the origin was given by

$$c = c_{max}\exp(-\frac{r^2}{\sigma_r^2}) \tag{4.1}$$

where

$$r = \sqrt{(x - x_0)^2 + (y - y_0)^2} \tag{4.2}$$

In Microsoft Excel, a normal distribution of one dimension has been defined in a built-in function normdist, in which

$$normdist(r, 0, \sigma_e, false) = \frac{1}{\sqrt{2\pi}\sigma_e} e^{-\frac{r^2}{2\sigma_e^2}} \tag{4.3}$$

Specifying an estimate for the location of the center of the distribution (x_0, y_0), and using Equations 4.1 and 4.2, 2-D Gaussian concentration distribution was fit by

$$c_{fit}(r(x_0, y_0), \sigma_e) = c_{max}\sqrt{2\pi}\sigma_e normdist(r, 0, \sigma_e, false) \tag{4.4}$$

Therefore σ_e, x_0 and y_0 in Equation 4.4 were used as fitting parameters for the sediment distribution, center (x_0, y_0), and characteristic spread. In the current experiments the distribution of sediment was expected to be axisymmetric, i.e. the 1-D variances σ_x and σ_y should be equal. Taking $\sigma_x = \sigma_y = \sigma_e$, the radial spread was therefore

$$\sigma_r = \sqrt{\sigma_x^2 + \sigma_y^2} = \sqrt{2}\sigma_e \tag{4.5}$$

The fitting values were chosen to minimize the least squares difference between the points on the analytical curve and the corresponding measured value at the same radii, i.e. the expression $\sum_{i=1}^{126} |(c_{i,fit}(\sigma_e, x_0, y_0))^2 - c_{i,measured}^2|$ was minimized. Figure 4-1 shows a sample of a fit of the 2-D Gaussian with the measured sediment spread, and Table 4-3 presents the accuracy of the Gaussian fits to the distribution. From the results it was found that the least square differences between the original data points and the fitting curves were minimal, once again justifying the Gaussian assumption. To conclude this section, Figure 4-2 shows the distributions of all eight glass beads used in the current experiments for a general perspective.

	least square difference
A	0.869
B (1)	0.838
B (2)	1.052
B (3)	0.570
C	0.407
D	0.201
AD	0.303
AE	0.094
AG (1)	0.053
AG (2)	0.026
AG (3)	0.086
AH	0.029

Table 4-3: The least square difference between the Gaussian fit and experimental data for each experiment.

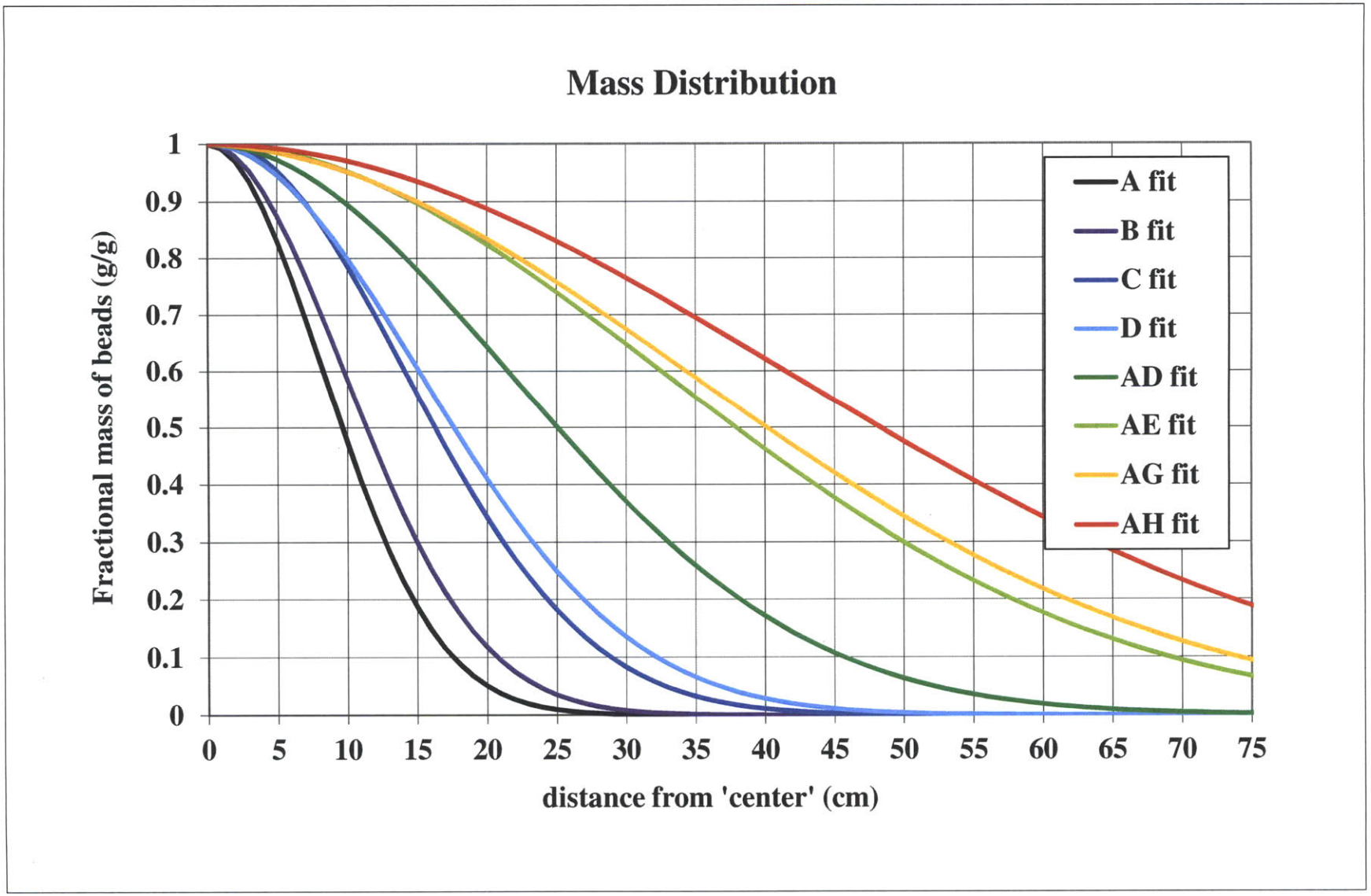

Figure 4-2: 2-D Gaussian fits with the measured sediment spread for each particle size.

4.3. Observations and proposed addition to plume classification

To further understand the relationship between plume spread and particle size, the relation between the standard deviation and U_N is plotted. Figure 4-3 shows the values of σ/H versus U_N for the eight respective particle size studied in the current experiments. It was found that the relationship follows a power curve in which σ/H decreases as U_N increases.

With visual observation on the development of the plume and comparison with the typology described by previous researchers (Socolofsky & Adams [45]), it was discovered that the typology was not sufficient to fully describe the behavior of the plumes observed in our current experiments. In particular, visual observations from current experiments revealed that particles in Type 1* multi-phase plume experienced detrainment from the plume but not necessarily intrusion while the liquid phase underwent intrusion. In some Type 1* plumes, particles temporarily followed the detraining fluids into the intrusion layers but eventually returned to the core plume and trailed the projection to the bottom. In other trails, particles detrained and intruded into the trapping layers, eventually falling outside of the core plume.

It was therefore proposed that a new plume type be defined to distinguish the two behaviors exhibited within the plume Type 1*. Type 1a* shall describe plumes with particle intrusion and fall out, and Type 1b* shall portrait plumes in which there is liquid detrainment but no particle intrusion.

Experimental results determined that Type 1a* plume behavior is observed for $U_N < 0.3 \pm 0.1$, based on visual observations shown in Figure 4-4. The cutoff U_N between Type 1a* and 1b* was set to be 0.3 ± 0.1 because it was observed that particle size D ($U_N = 0.4$) exhibited Type 1b* plume structure with no plume peeling, while particle size AD ($U_N = 0.2$) demonstrated Type 1a* plume structure with plume trapping and peeling. To complete the typology, experimental observations from Socolofsky and Adams [45] are included, suggesting plume Type 1a* for $0 < U_N < 0.3 \pm 0.1$, Type 1b* for $0.3 \pm 0.1 < U_N < 1.2$, Type 2 for $1.2 < U_N < 2.4$, and Type 3 for $U_N > 2.4$, as shown in Figure 4-5.

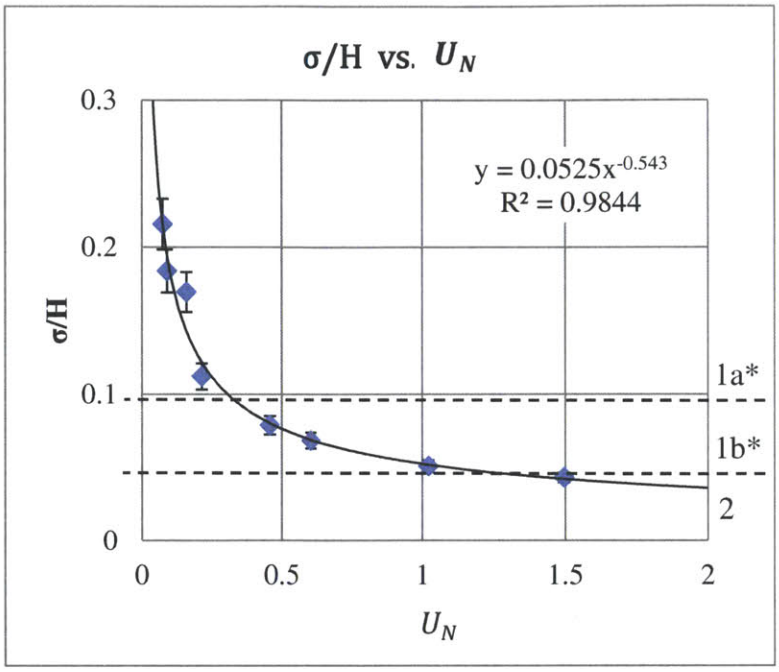

Figure 4-3: σ/H vs. U_N

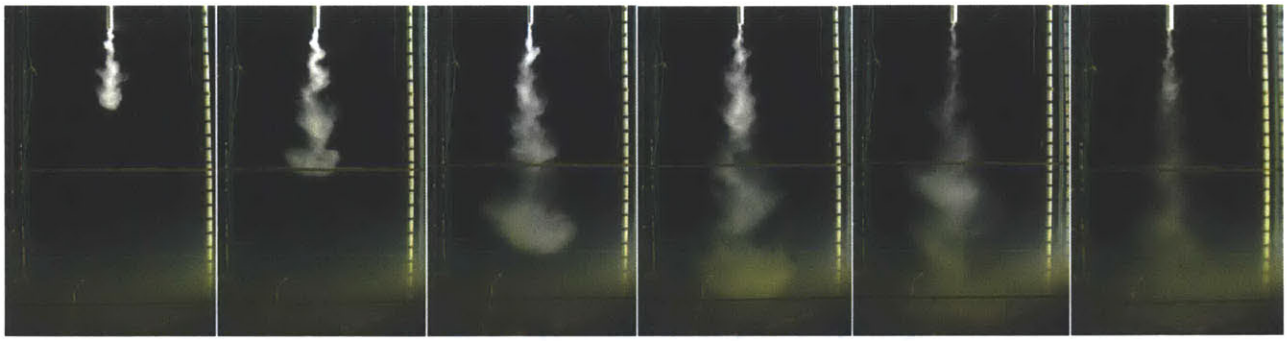

Figure 4-4(a): Experimental observation for particle size D ($U_N = 0.4$)*

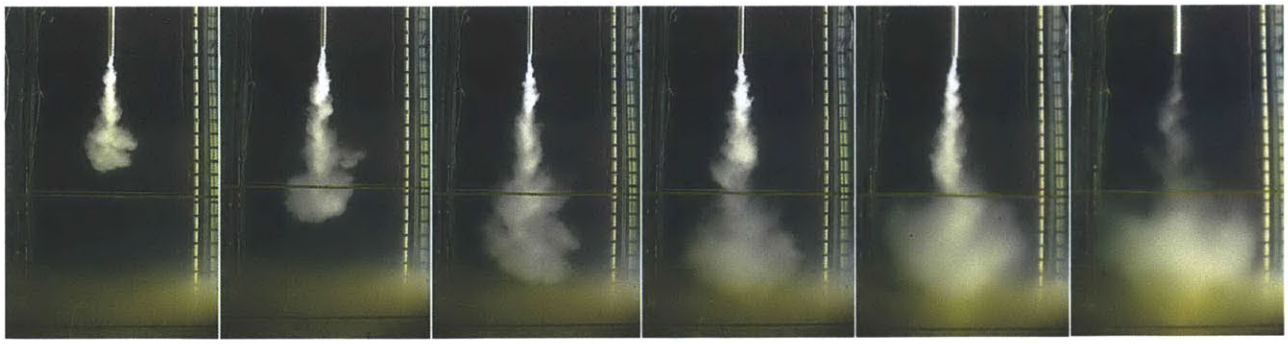

Figure 4-4(b): Experimental observation for particle size AD ($U_N = 0.2$)*

*Please note that in Figure 4-4 the time frames of the two set of pictures do not match exactly.

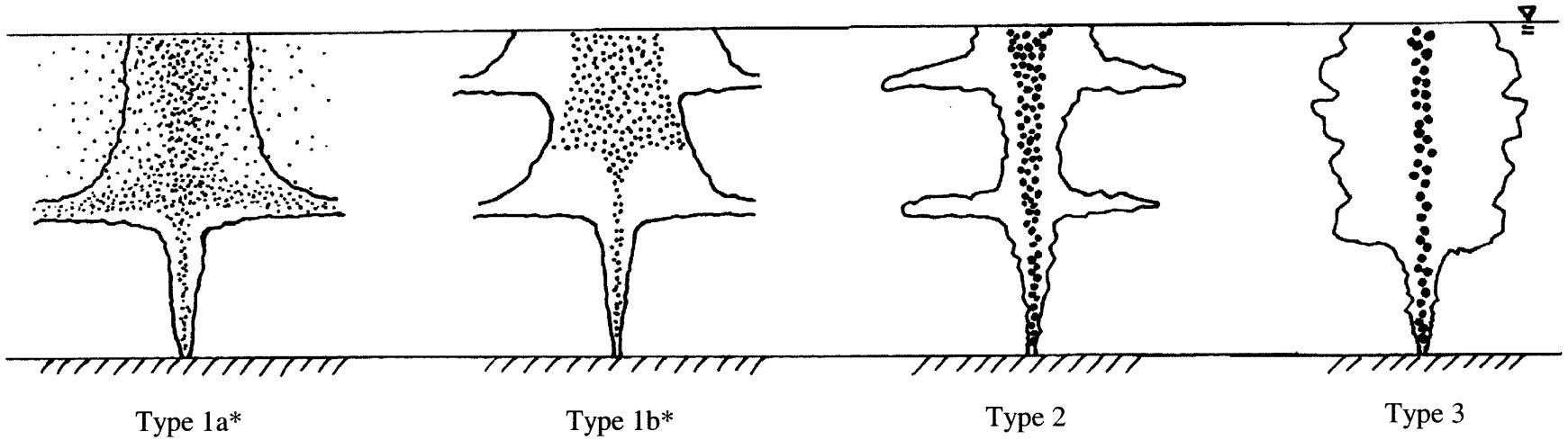

Figure 4-5: New typology for stagnant multi-phase plume structure derived from the current experiments.

4.4. Comparison to well-mixed model and past experiments

Experimental results obtained from the current experiments are compared to the well-mixed model as suggested in Section 2.2.5. An empirical relationship between the particle spread σ_r and various parameters determining the plume structure including buoyancy flux B, stratification frequency N and slip velocity u_s, as stated in Equation 2.26.

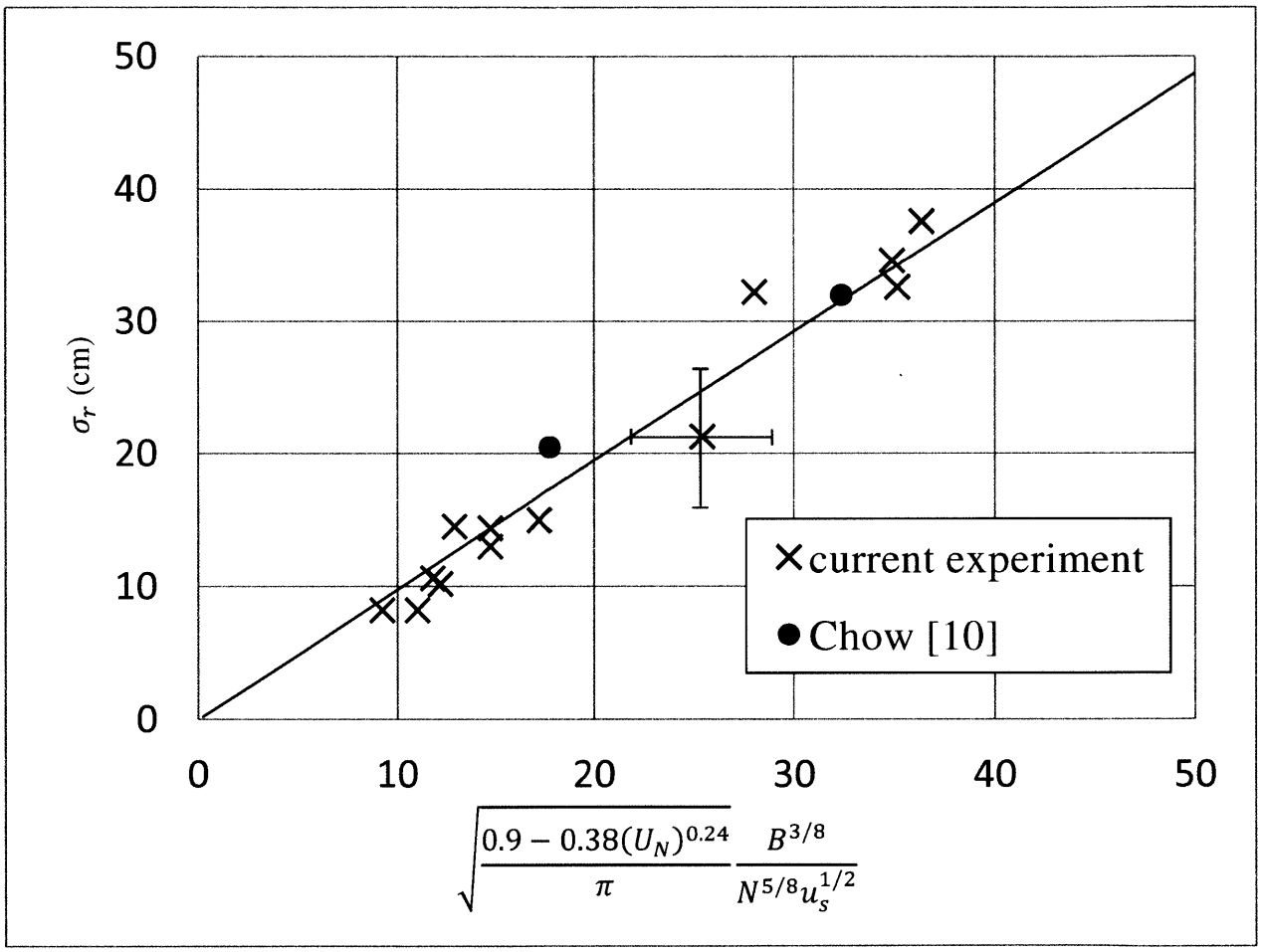

Figure 4-6: Empirical relationship between particle spread and experimental parameters for experiments with one bead size.

It was observed that there exists a linear relationship as shown in Figure 4-6. This indicates that the well-mixed model closely predicts experimental outcomes, suggesting particles within the intrusion layer radiate outwards from the centerline of the plume in a Gaussian manner, and the model can be used to predict the spread of the particles. Experimental data from Chow [10] were also plotted for comparison. The two data points from Chow [10] were single size releases

experiment with size AE and AH respectively. Chow's experimental data were slight adjusted to include the effects of non-dimensional slip velocity in the x-axis, and the slip velocities of the current experimental conditions were used. From Figure 4-6, the current experimental results closely resembles the trend exhibited by Chow [10], thus corroborating the accuracy of the current experiments.

4.5. Experiment with beads of different sizes

The current experiments also include a series of trials in which particles of two difference size were released simultaneously into the water tank. The goal of these runs was to study if interaction between two particle sizes within a muti-phase plume affects the radial particle spread. This investigates behavior of a multi-phase plume when two or more sizes of oil droplets are present at the same time. Five experiments were conducted in which three conditions were included. One condition was repeated three times to verify the repeatability of this experiment. Tables 4-4 to 4-6 show the data collected in all seven trials in detail.

The first condition explored in the current experiments involves the mixing of a Type 1a* (Size AG) and Type 1b* (Size B) particles. Three trials were conducted and the results are listed in Table 4.4. The results acquired from the single size releases for Size B and AG are also listed for comparison. Standard errors of the experiment were calculated and compared to the difference between the averages of single size releases and two size releases. From the table it was observed that the interaction between two particle size has minimal or no impact on the radial spread of the particles. There exists only a slight reduction of spread for the larger particles when both sizes are released simultaneously, while the smaller particles maintains it original spread.

Two additional experiments include another run with beads with Type 1a* behavior (Size AG) mixed with Type 1b* behavior (Size D), and an additional run with interaction between two beads with Type 1b* behavior (Size B & D). The results are presented in Table 4.5 and 4.6. According to the results, interactions between two particle sizes continue to show minimal effects on radial spread.

In general, the results suggest that releasing two particle sizes simultaneously has minimal or no effects on radial particle spread. Plotting experimental data from experiments with different beads sizes together with single bead size further confirm the hypothesis that releasing different

particle sizes together has little effect on particle spread (Figure 4-7). This suggests that for a practical situation, a single particle size can be isolated from a range of sizes for studying its radial particle spread.

Particles	σ_r (cm)	$\overline{\sigma_r}$ (cm)	Standard Error	Difference between averages (cm)
B	8.2	9.667	0.742	1.100
B	10.6			
B	10.2			
B (2)	8.8	8.567	0.186	
B (2)	8.2			
B (2)	8.7			
AG	34.6	34.933	1.453	-0.233
AG	37.6			
AG	32.6			
AG (2)	33.9	35.167	1.419	
AG (2)	33.6			
AG (2)	38			

Table 4-4: Two-beads experiment between particle size B & AG.

Particles	σ_r (cm)	$\overline{\sigma_r}$ (cm)	Standard Error	Difference between averages (cm)
B	8.2	9.667	0.742	0.567
B	10.6			
B	10.2			
B (2)	9.1	9.1	-	
D	15	15	-	0.600
D (2)	14.4	14.4	-	

Table 4-5: Two-beads experiment between particle size B & D.

Particles	σ_r (cm)	$\overline{\sigma_r}$ (cm)	Standard Error	Difference between averages (cm)
D	15	15	-	0.500
D (2)	14.5	14.5	-	
AG	34.6	34.933	1.453	-1.667
AG	37.6			
AG	32.6			
AG (2)	36.6	36.6	-	

Table 4-6: Two-beads experiment between particle size D & AG.

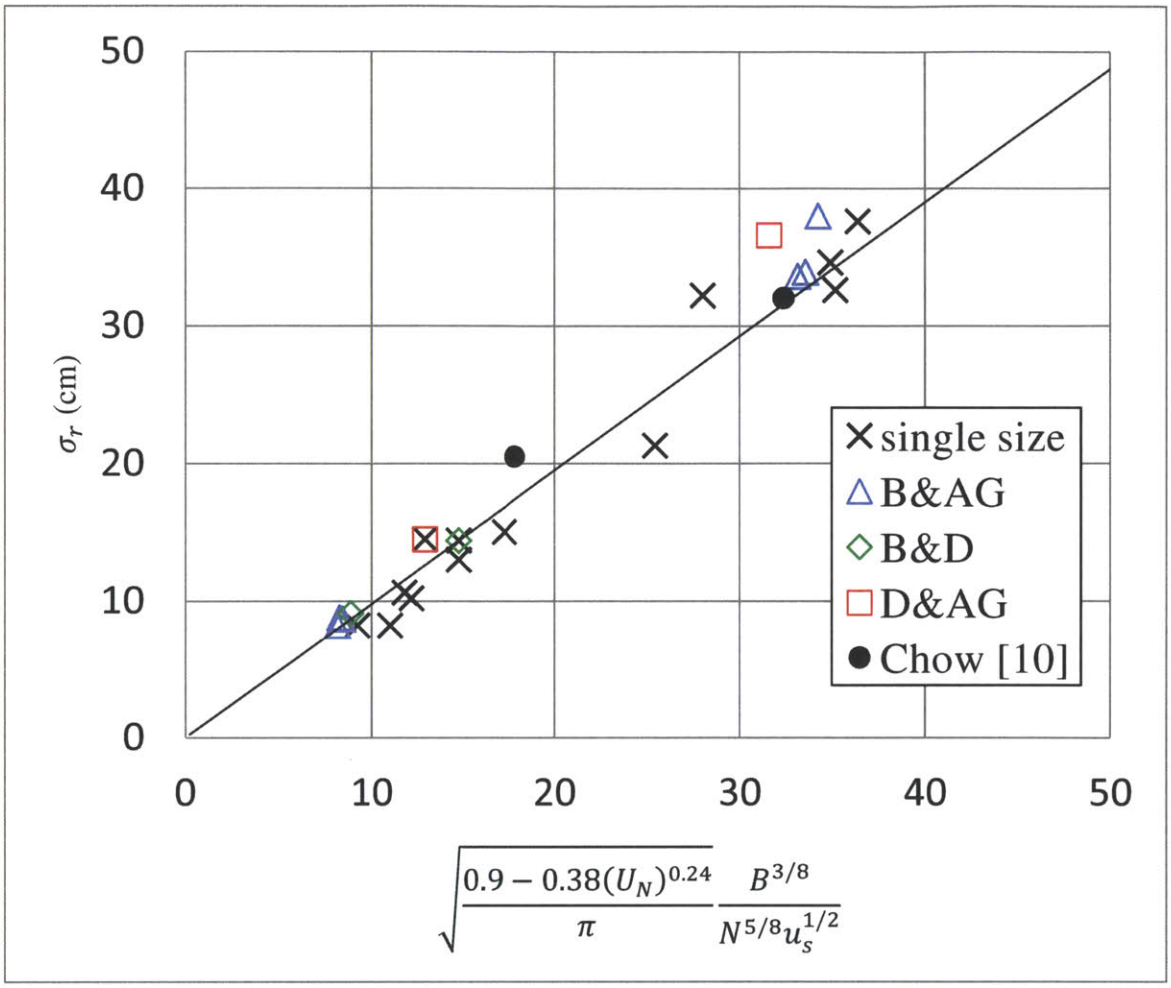

Figure 4-7: Empirical relationship between particle spread and experimental parameters including experiments with two bead sizes.

4.6. Application to real scenarios

To understand the relationship between the experimental results and real world scenarios, the current theory was applied using data acquired from two previous settings, including the 'Deep Spill' experiment conducted in 2000 and the Deepwater Horizon oil spill in 2010. From the previous sections, it was concluded that the spread of particles or droplets σ_r in a positively buoyant plume can be predicted using the non-dimensional slip velocity U_N, which requires information including the buoyancy flux B, stratification frequency N and the droplet slip velocity u_s. The buoyancy flux B amd stratification frequency N of the Deep Spill experiment and Deepwater horizon oil spill is presented in Table 4-7.

	Deep Spill	Deepwater Horizon
Buoyancy flux, B (m^4/s^3)	0.095	0.73
Stratification frequency, N (1/s)	0.0015	0.00155

Table 4-7: Buoyancy flux and stratification frequency for Deep Spill experiment and Deepwater Horizon oil spill (Johansen et al. [25], Socolofsky et al. [46])

The slip velocities of the droplets are calculated using the relationship presented in Zheng and Yapa [55], which will be discussed later in this section.

A graphical representation of the relationship between σ_r and U_N can be constructed and the curves can be divided into three sections, describing three different plume structures: 1) Type 1a* ($U_N \leq 0.3$), 2) Type 1b* ($0.3 < U_N \leq 1.4$), and 3) Type 2 ($1.4 < U_N$).

1) For $U_N \leq 0.3$, when particles are shown to intrude and exhibit Type 1a* behavior, the standard deviation σ_r of the spread of the droplets can be predicted by Equation 2.26:

$$\sigma_r = \sqrt{\frac{0.9 - 0.38(U_N)^{0.24}}{\pi}} \frac{B^{3/8}}{N^{5/8} u_s^{1/2}} \tag{4.6}$$

This relationship was used to obtain the solid lines for $U_N \leq 0.3$ for both real world scenarios in Figure 4-9.

2) For $0.3 < U_N \leq 1.4$, the well-mixed model (Equation 4.6) can be applied again to predict the relationship between σ_r and U_N. As mentioned in Section 2.2.5 the model was assumed to be valid only for U_N much smaller than 1; however, the current experiments with U_N spanning between 0.07 and 1.5 shown a linear relationship between the standard deviation of particle spread and Equation 4.6. This suggest the model can closely describe the relationship between σ_r and U_N up to $U_N \leq 1.5$. This allows us to extrapolate the relationship into the Type 1b* region and plot the dashed lines for the relationship between σ_r and U_N in Figure 4-9.
3) Finally, for $U_N > 1.4$, the spread of the dispersed phase within a plume was determined using experimental results acquired from Socolofsky and Adams [44], who presented research of

the ratio, λ, of bubble width, σ_r, to plume width σ_p for bubble plumes. The relationship between λ and U_N, derived in Socolofsky and Adams (Figure 3-8) [44], is shown below in Figure 4-8.

The plume spread can be evaluated at the trap height h_T giving:

$$\sigma_p = \varepsilon h_T \tag{4.7}$$

with the trap height h_T discussed in Equation 2.14:

$$h_t = 2.8\left(\frac{B}{N^3}\right)^{1/4} \tag{4.8}$$

Therefore, the characteristic spread of particle or droplets σ_r can be describes as:

$$\sigma_r = \lambda\sigma_p = 2.8\lambda\varepsilon\left(\frac{B}{N^3}\right)^{1/4} \tag{4.9}$$

Because Socolofsky and Adams' work focused on plume Type 2 or larger, their results allowed us to determine the relationship between σ_r and U_N for $U_N > 1.4$. Setting $\varepsilon = 0.172$ *and* 0.16 for Deepwater Horizon and 'Deep Spill' scenario respectively, the solid lines in the region $U_N > 1.4$ are obtained. Thus we can achieve a full relationship between σ_r and U_N for all three plume types, 1a*, 1b* and 2, as shown in Figure 4-9.

From Figure 4-9, it was observed that σ_r remains relatively constant for Type 1b* and Type 2 plumes ($U_N > 0.3$), while σ_r increases rapidly as U_N becomes smaller and smaller for Type 1a* plumes ($U_N \leq 0.3$). This suggests that in the event of an oil spill, it is desirable to achieve plume Type 1a* to maximize oil droplet spread, allowing easier degradation of oil droplets and greater dilution of the oil. Applying dispersants to the spill is one effective way to reduce droplet diameter.

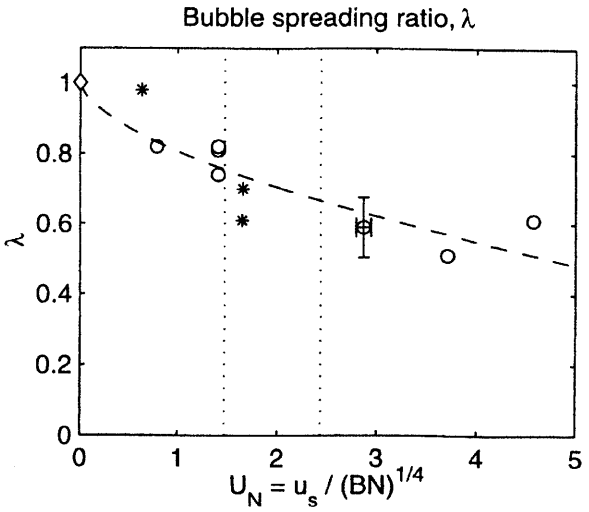

Figure 4-8: Bubble spreading ratio vs. U_N (Socolofsky and Adams [44])

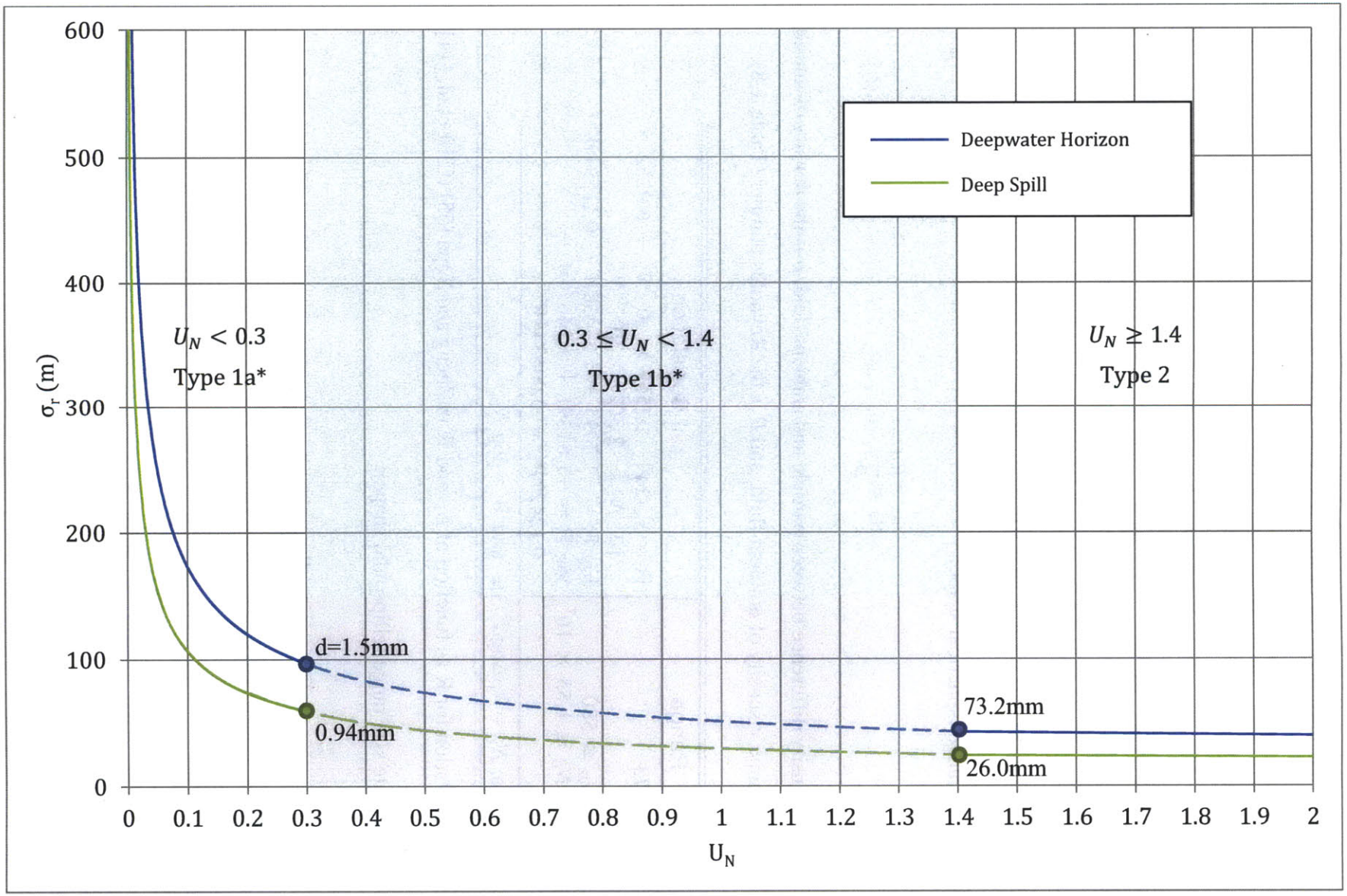

Figure 4-9: Standard deviation of droplet spread versus non-dimensional slip velocity in Deepwater Horizon and Deep Spill scenario.

To further apply the current experimental results in real world conditions, the relationship between the standard deviation of droplet spread σ_r with the droplet diameter d was estimated for each plume structure type. Previous research has shown that the shape of fluid particles (gas bubbles and liquid drops) in most systems can be classified in three different sizes: 1) a sphere in the small size range ($d_e \leq 1\ mm$), an ellipsoid in the intermediate size range ($1\ mm < d_e \leq 15\ mm$), and a spherical-cap in the large size range ($d_e > 15\ mm$), with d_e = equivalent particle diameter (Clift et al. [11], Haberman & Morton [18], Takemura & Yabe [48], Zheng & Yapa [55]). The relationship between slip velocity u_s and diameter of particle d are as follows:

1) For small size range (spherical shape):

$$u_s = \frac{R\mu}{\rho d} \tag{4.10}$$

where $\Delta\rho$ is the density difference between particle and ambient fluid, ρ is the density of ambient fluid, μ is the dynamic viscosity of ambient fluid, and R is the Reynolds number (Table 4-8).

Range	Correlation
$N_D \leq 73$	$\mathrm{R} = N_D/24 - 1.7569 \times 10^{-4} N_D^2 + 6.9252 \times 10^{-7} N_D^3 - 2.3027 \times 10^{-10} N_D^4$
$73 < N_D \leq 580$	$\log \mathrm{R} = -1.7095 + 1.33438W - 0.11591W^2$
$580 < N_D \leq 1.55 \times 10^7$	$\log \mathrm{R} = -1.81391 + 1.34671W - 0.12427W^2 + 0.006344W^3$
Note: $N_D = 4\rho\Delta\rho g d_e^3/3\mu^2$ and $W = \log N_D$.	

Table 4-8: Correlation for R as function of N_D and W in Zheng and Yapa [55] (Clift et al. [11])

2) For intermediate size range (ellipsoidal shape):

$$u_s = \frac{\mu}{\rho d_e} M^{-0.149}(J - 0.857) \tag{4.11}$$

where

$$J = 0.94H^{0.757}, \qquad (2 < H \leq 59.3) \tag{4.12}$$

$$J = 3.42H^{0.441}, \qquad (H > 59.3) \tag{4.13}$$

and

$$H = \frac{4}{3} EoM^{-0.149} \left(\frac{\mu}{\mu_w}\right)^{-0.14} \tag{4.14}$$

in which μ_w is the dynamic viscosity of water, and M and Eo are defined as:

$$M = g\mu^4 \Delta\rho / \rho^2 \sigma^3 \tag{4.15}$$

$$Eo = g\Delta\rho d_e^2 / \sigma \tag{4.16}$$

3) For large size range (spherical–cap):

$$u_s = 0.711\sqrt{g d_e \Delta\rho / \rho} \tag{4.17}$$

Figure 4-10 shows the relationship between σ_r and d by transforming the non-dimensional slip velocity U_N into d through the relationship between slip velocity u_s and d. The solid lines in Figure 4-10 shows the relationship between σ_r and d assuming spherical particles ($d_e \leq 1\ mm$), and the dashed lines demonstrate σ_r and d assuming ellipsoidal particles ($1\ mm < d_e \leq 15\ mm$).

The results from Figure 4-10 demonstrates that if the sizes of the droplets are smaller than 1mm, reducing droplets sizes is very effective in increasing the droplet spread. This suggests that applying dispersants in an oil spill scenario can be beneficial in remediating the pollution, assuming that smaller oil droplets are easier to degrade in the environment and spread more, results in greater dilution of the oil.

For example, taking an oil spill scenario with a known range of oil droplets diameter, the initial standard deviation of droplet spread $\sigma_{r,0}$ can be found by Figure 4-10, assuming quiescent conditions with no crossflow current. If dispersants were applied to reduce the droplets diameter, a new value for the standard deviation of droplet spread $\sigma_{r,new}$ can be found in Figure 4-10, reflecting the reduction in oil droplets sizes that can be achieved by applying dispersants.

Ongoing research on the effects of dispersants on oil droplet sizes demonstrates that dispersants are capable of reducing sizes of oil droplets in a case of the oil spill. However, limited data are available for sub-surface applications of dispersants on oil pill plumes. To demonstrate the

importance of achieving smaller droplet size in oil droplets dispersion for a deepsea oil spill, a hypothetical example is presented below:

Conditions from the Deep Spill experiment are assumed where the initial diameters of undispersed oil droplets ranged between 1000 to 10000 microns (Johansen et al. [25]). Assuming that dispersants reduce the sizes of oil droplets to 1/10 of their original sizes, the initial and final standard deviation of the droplet spreading distance $\sigma_{r,0}$ & $\sigma_{r,new}$ can be determined from the relationship illustrated in Figure 4-10. Similar results are obtained for the Deepwater Horizon oil spill assuming the same droplet sizes distributions with and without dispersants. The results for the droplet spreading distance for both scenarios are presented in Table 4-9:

	$\sigma_{r,0}$ (No dispersants)		$\sigma_{r,new}$ (With dispersants)	
	Minimum	Maximum	Minimum	Maximum
Deepwater Horizon	58	110	110	800
Deep Spill	25	50	50	400

Table 4-9: Comparison of droplet spreading distance between Deepwater Horizon and Deep Spill

From Table 4-9 it was found that the increase in the maximum droplet spreading distance for both scenarios was approximately 8 times the original spreading distance. A graphical illustration for this example is shown in Figure 4-11.

In a real world scenario, the increase in the *droplet spreading area* scales as the square of the increase in the standard deviation of the droplet spread σ_r. In the current examples, the increase in *maximum droplet spreading areas* due to application of dispersants is thus approximately $8^2 = 64$ times the initial values respectively. Furthermore, dispersed droplets reaching the surface will be subjected to further dispersion due to energy input from breaking waves and wind. And smaller droplets spreading over a large area will be more easily dispersed than larger droplets spread over a small area. Therefore, the increases in spreading areas for the current examples are likely to be greater than the current computed magnitudes. This shows the effect of reducing droplet diameter in increasing droplet spread when dispersants are applied to potential oil spill.

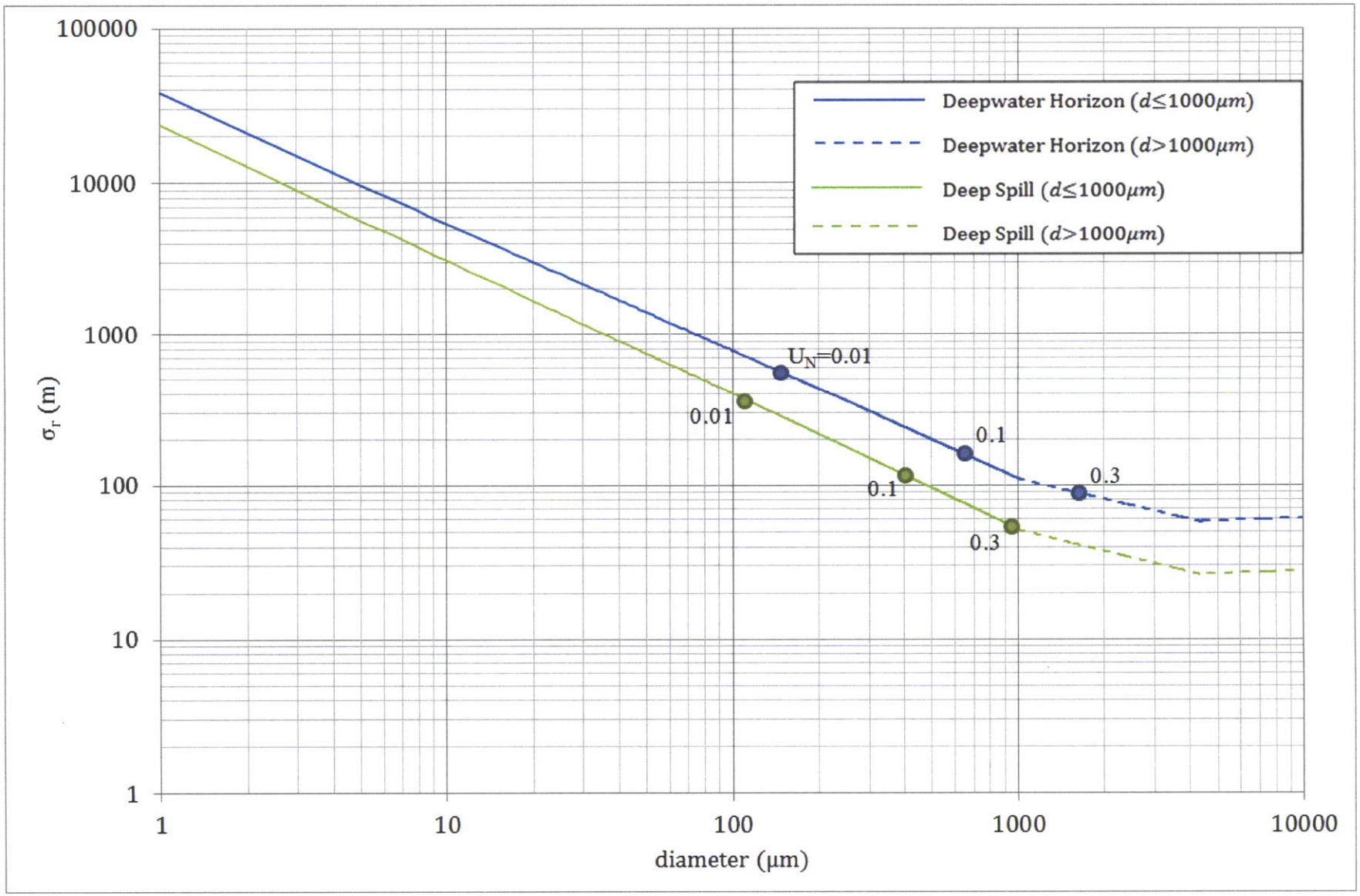

Figure 4-10: Standard deviation of droplet spread versus diameter of droplets in Deepwater Horizon and Deep Spill scenario.

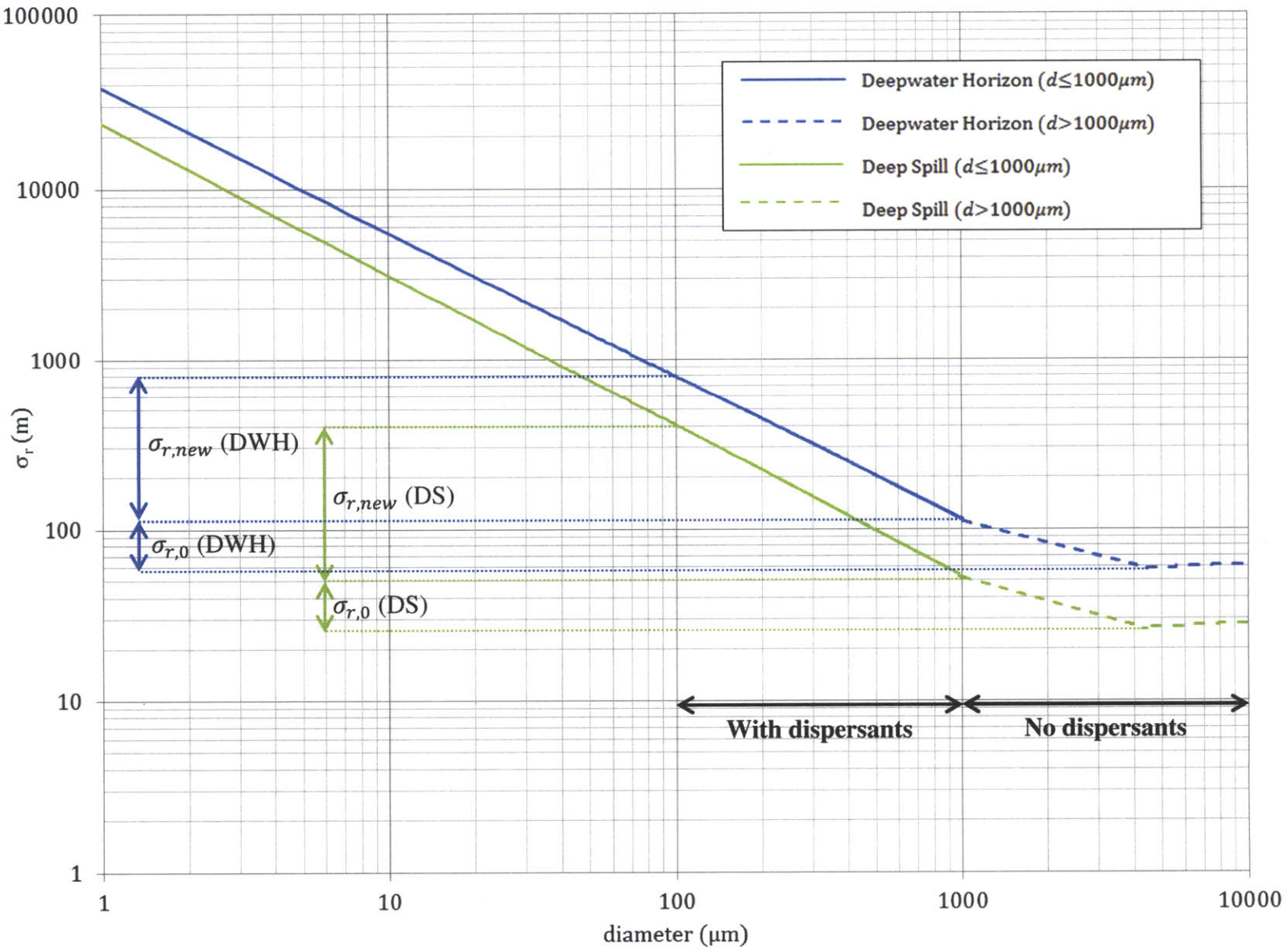

Figure 4-11: Comparison of standard deviation of the droplet spreading distance between Deepwater Horizon and Deep Spill scenario

4.7. Error analysis

There exist three main types of experimental error: measurement error, systemic error and random error. Measurement errors relate to the resolution of the equipment and the repeatability of the measurement. Systemic errors are generally caused by calibration and observational errors. Random errors are due to unbiased statistical scatter around the measured value, and can be determined by repeating the experiment a certain number of times.

4.7.1. Measurement errors

Particle Flow Rate

The particle flow rate of glass beads was calculated based on the measured time to empty the flask in the release mechanism. It also depends on the scale used to measure the weight of the total amount of glass beads sued in each experiment. The measurement resolution of the scale was ±0.01 g and the stopwatch ±0.01 s. The standard deviations of the flow rates, obtained for similar experimental conditions, were used as the error of particle flow rate.

Sediment spread

The sediment spread, σr, was a fitted 2-D Gaussian standard deviation of 126 different mass measurements at various horizontal coordinates. The center of the distribution and the variance were picked out so as to yield the least squares difference with the recorded sediment masses.

Some of the experimental radial distributions, though Gaussian in shape, appeared to have a different spread in different directions, suggesting an azimuthal variation. This may be due to the plume meandering, improper centering or directing of the initial plume source. It may be due to the fact that the experiments were performed in a confined tank, which can potentially introducing secondary circulation, while the modeled physical scenario is an unconfined ambient. All of these factors would have caused a deviation of the resulting sediment distribution from a Gaussian or axisymmetric distribution.

4.7.2. Errors in calculated quantities

Errors in calculated quantities stem from the measured quantities: if a calculated quantity F, is calculated from n measurements, i.e.:

$$F = f(x_1, x_2, \ldots, x_n) \tag{4.18}$$

then, with each error δx_n, the total error in F, δF, is calculated using the measurement error equation:

$$\delta F = \sqrt{\sum_{i=1}^{n} \left(\left(\frac{\partial f}{\partial x_i} \right) \delta x_i \right)^2} \tag{4.19}$$

The calculated quantities in an experiment are B_s the brine buoyancy flux, B_b, the particle buoyancy flux, N.

$$\delta N = \sqrt{\frac{g(\delta\rho)^2}{4\rho(\rho_1 - \rho_2)(z_1 - z_2)} + \frac{g(\rho_1 - \rho_2)(\delta z)^2}{4\rho(z_1 - z_2)^3}} \tag{4.20}$$

$$\delta N = \sqrt{\left(\frac{g(\rho - \rho_b)^2}{\rho} \delta Q_b \right)^2 + \left(\frac{g Q_b}{\rho} \delta \rho_b \right)^2} \tag{4.21}$$

Slip Velocity

An empirical relation (Equation 3.4) is used to relate slip velocity to the diameter and density of the particles used. Assuming negligible error of the equation itself and of the density, the source of error will be from the particle diameters. The error can simply be estimated by applying Equation 3.4 to each size distribution obtained by sieve analysis, and in particular to diameters one standard deviation from the mean diameter used.

Quantity	Error
u_s (m/s)	±3E-05
B (m^4/s^3)	±1.42E-06
N (1/s)	±7.87E-03

Table 4-10: Experimental error in slip velocity, buoyancy flux and stratification frequency

5. Conclusion and future work

The effects of droplet size on intrusion of sub-surface oil spills were studied experimentally by modeling oil plumes with glass beads in a stratified tank. The results of the experiments were compared with empirical relationships and past experiments. The measurement of interest is the radial particle spread of particles due to plume intrusion in each experiment. Experimental conditions including initial buoyancy flux, stratification frequency and particle slip velocity are the main variables in determining the radial particle spread for each particle size.

From the experimental results, it was observed that the particle distribution for a multi-phase plume can be described as a Gaussian distribution. This implies that a well-mixed intrusion layer is depositing the sediment to the bottom, under the condition $U_N \leq 1.5$. Results from experiment with a single bead size also deduced that the standard deviation of the radial particle spread σ_r is related to the non-dimensional slip velocity U_N by a power function. Further investigation suggested that the standard deviation of the distribution can be predicted as a function of total initial buoyancy flux B, stratification frequency N, the particle velocity u_s, and the non-dimensional slip velocity $U_N = \frac{u_s}{(BN)^{1/4}}$, which depends on all three parameters stated above.

$$\sigma_r = \sqrt{\frac{0.9 - 0.38(U_N)^{0.24}}{\pi}} \frac{B^{3/8}}{N^{5/8} u_s^{1/2}} \tag{5.1}$$

A new typology was proposed to describe plume structures with $U_N \leq 1.4$. The proposed new classification suggesting plume Type 1a* for $0 < U_N < 0.3 \pm 0.1$, Type 1b* for $0.3 \pm 0.1 < U_N < 1.2$, Type 2 for $1.2 < U_N < 2.4$, and Type 3 for $U_N > 2.4$, are shown in Figure 4-5.

Experiments with beads of difference sizes also suggested that the interaction between two particle groups has minimal effects on their radial particle spread. This indicates that particles of difference sizes can be treated independently when analyzing their radial plume spread.

The knowledge acquired from the experiments can be applied to real life scenario. Assuming the best course of action for an oil spill scenario is to achieve as much particle spread as possible for environmental and sociological purpose, and dispersants were decided to be applied to increase particle spread; the current experiment provides a reference on what is the minimum diameter

needed to achieve by applying dispersants for efficient particle spread. The desired threshold will be achieving Type 1a* plume structure for maximum plume spread. This indicates that by knowing the following parameters for a scenario: 1) initial flow rate, which relates to the buoyancy flux B; 2) the ambient stratification profile N; and 3) the properties of the spilled particles, namely the slip velocities u_s; suitable amount of dispersants can be determined and applied to reduce the size of the particle exiting the spill, allowing them to intrude and spread for a larger distance in the ocean column. A hypothetical example with conditions taken from the 'Deep Spill' experiment and Deepwater Horizon oil spill was presented in Section 4.6.

Future work

While a relationship was established between radial particle spread and particle size, further work may involve exploring the interaction between particles of different densities, such as gas and oil particles. Laboratory experiments in larger scales or field experiments are also useful in studying the relationship of particle spread and sizes. Incorporating crossflow current in experimental study will also be beneficial in further understanding plume structure and particle spread.

A. Experimental Data

This appendix presents experimental data and results for each experiment.

A.1. Experiments with one single bead size

Size A

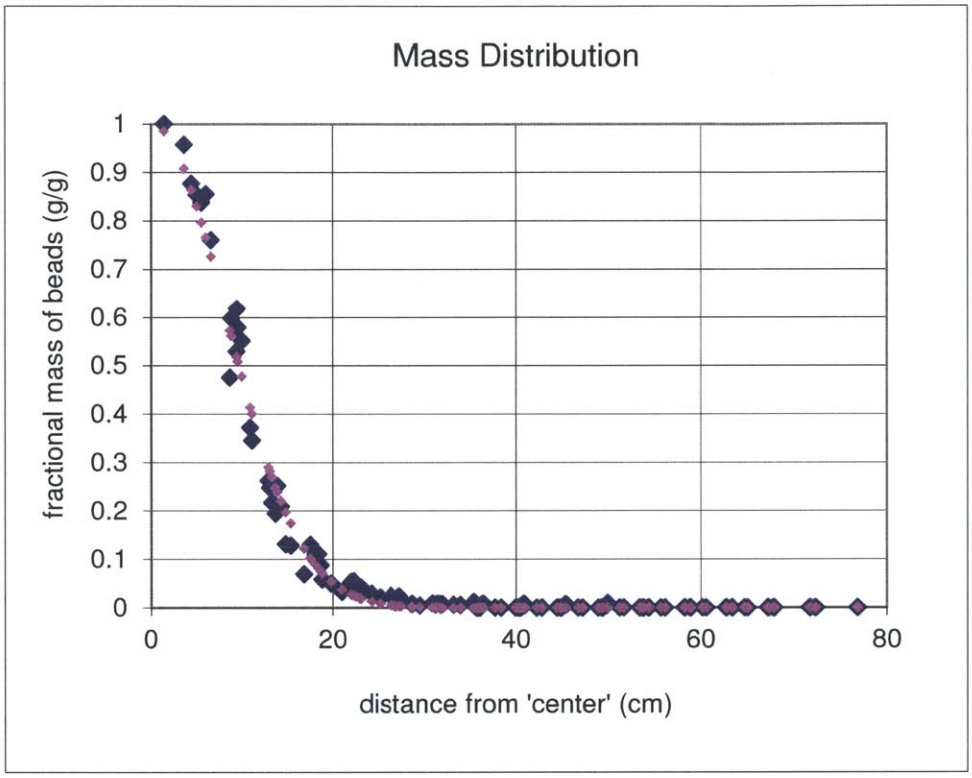

Figure A-1: Size A sediment radial distribution

Particles Median diameter (μm)	Mass released (kg)	Duration of release (s)	Q_b (m^3/s)	B (m^4/s^3)	N (1/s)
725	0.75	38	8.06E-06	1.15E-04	0.255
U_N	**Center x (cm)**	**Center y (cm)**	**sigma (cm)**	**least sq. difference**	**Kurtosis**
1.483	-4.80	1.10	8.20	0.869	0.203

Table A-1: Size A Experimental conditions and results

Size B(1)

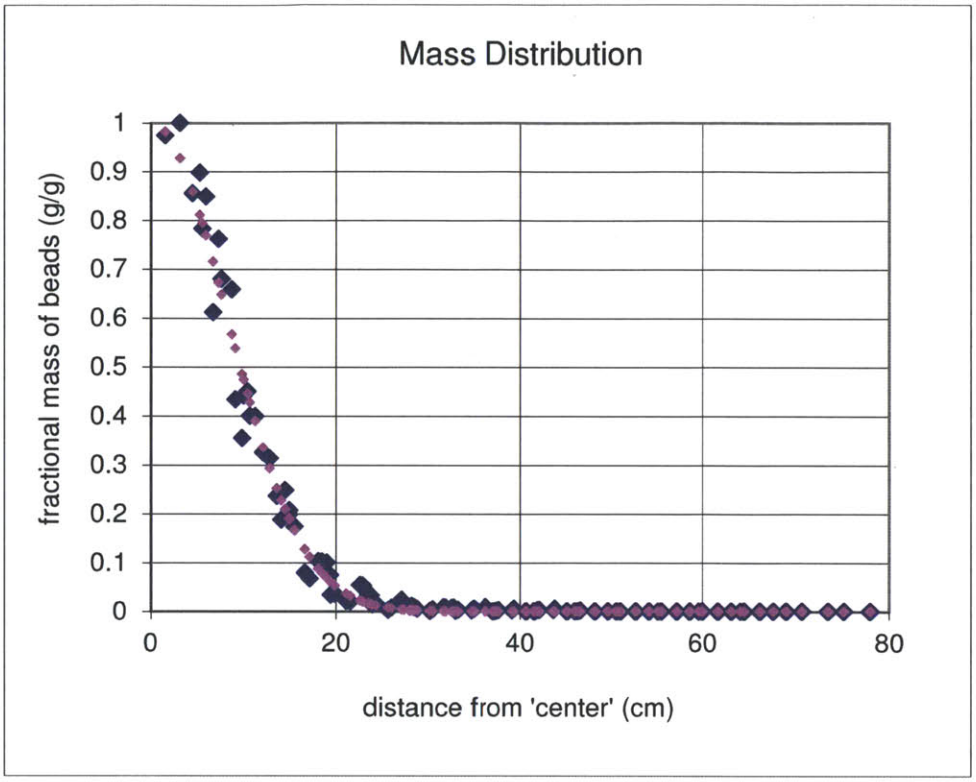

Figure A-2: Size B(1) sediment radial distribution

Particles Median diameter (μm)	**Mass released (kg)**	**Duration of release (s)**	**Q_b (m^3/s)**	**B (m^4/s^3)**	**N (1/s)**
512.5	1	55	7.42E-06	1.06E-04	0.263
U_N	**Center x (cm)**	**Center y (cm)**	**sigma (cm)**	**least sq. difference**	**Kurtosis**
1.025	-1.40	-1.80	8.20	0.838	-0.005

Table A-2: Size B(1) Experimental conditions and results

Size B(2)

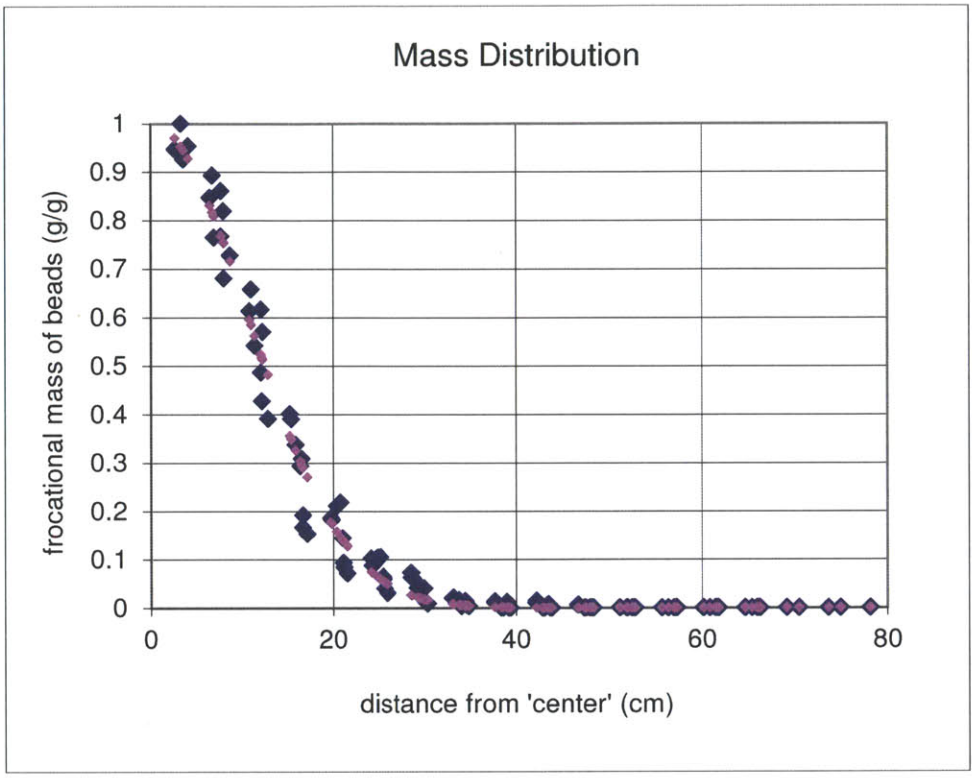

Figure A-3: Size B(2) sediment radial distribution

Particles Median diameter (μm)	**Mass released (kg)**	**Duration of release (s)**	**Q_b (m^3/s)**	**B (m^4/s^3)**	**N (1/s)**
512.5	1	50	8.16E-06	1.16E-04	0.25
U_N	**Center x (cm)**	**Center y (cm)**	**sigma (cm)**	**least sq. difference**	**Kurtosis**
1.014	1.60	-0.40	10.60	1.052	-0.101

Table A-3: Size B(2) Experimental conditions and results

Size B(3)

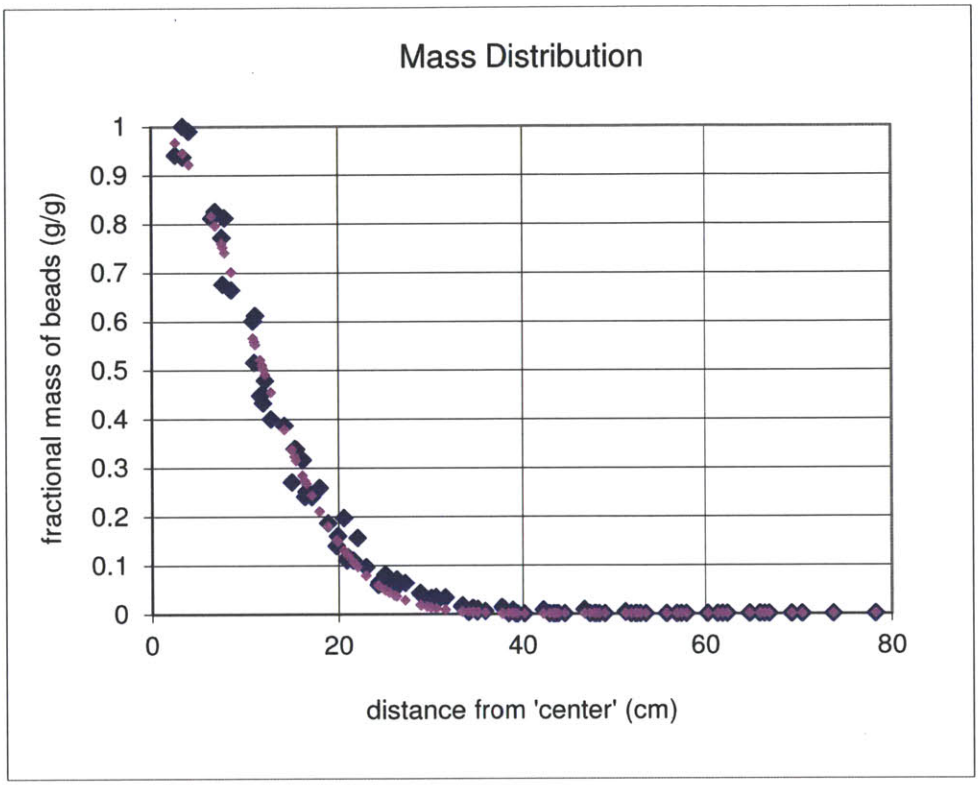

Figure A-4: Size B(3) sediment radial distribution

Particles Median diameter (μm)	**Mass released (kg)**	**Duration of release (s)**	**Q_b (m^3/s)**	**B (m^4/s^3)**	**N (1/s)**
512.5	1	45	9.07E-06	1.29E-04	0.254
U_N	**Center x (cm)**	**Center y (cm)**	**sigma (cm)**	**least sq. difference**	**Kurtosis**
0.984	-6.20	-0.50	10.20	0.570	0.000

Table A-4: Size B(3) Experimental conditions and results

Size C

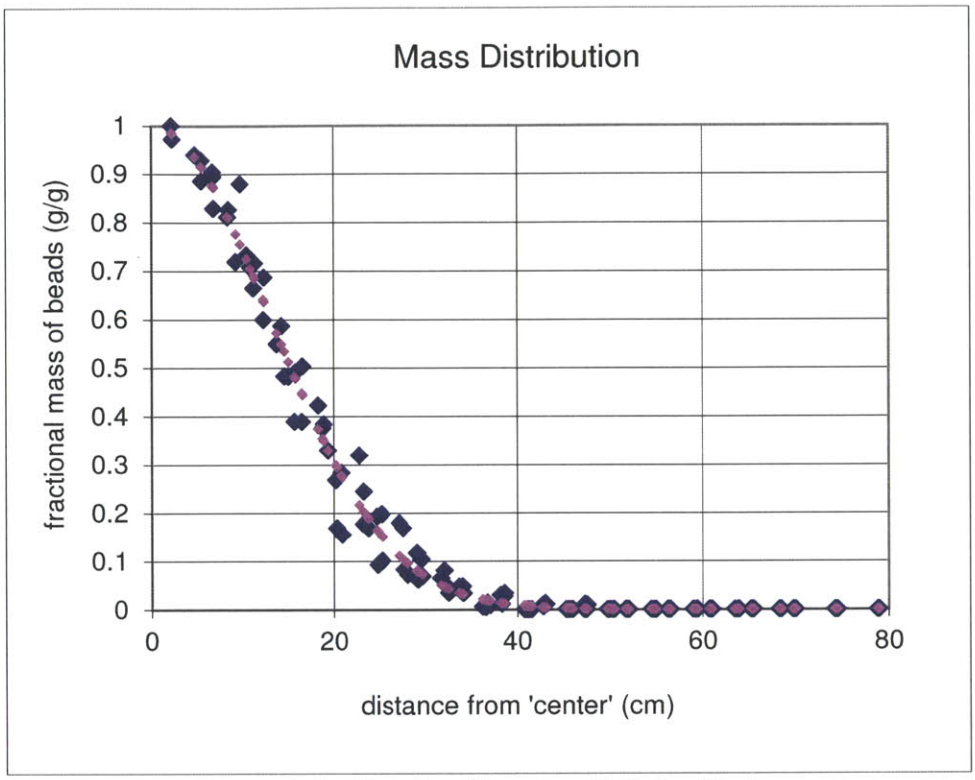

Figure A-5: Size C sediment radial distribution

Particles Median diameter (μm)	**Mass released (kg)**	**Duration of release (s)**	**Q_b (m^3/s)**	**B (m^4/s^3)**	**N (1/s)**
337.5	1	60	6.80E-06	9.70E-05	0.262
U_N	**Center x (cm)**	**Center y (cm)**	**sigma (cm)**	**least sq. difference**	**Kurtosis**
0.630	-2.30	-2.50	13.00	0.407	-0.182

Table A-5: Size C Experimental conditions and results

Size D

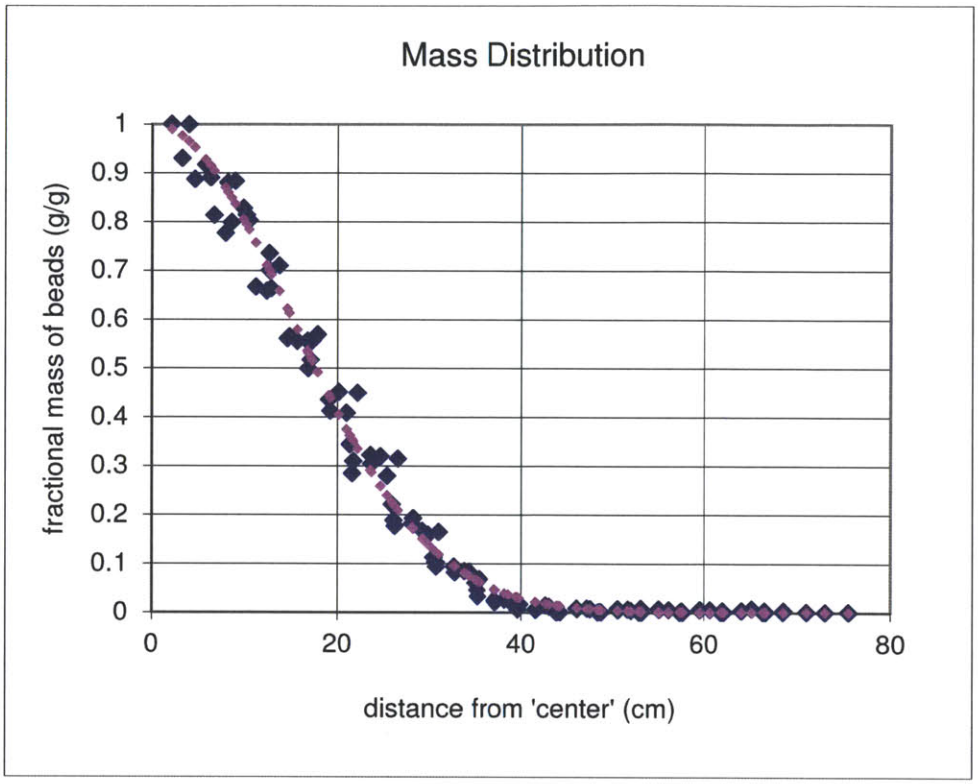

Figure A-6: Size D sediment radial distribution

Particles Median diameter (μm)	**Mass released (kg)**	**Duration of release (s)**	**Q_b (m^3/s)**	**B (m^4/s^3)**	**N (1/s)**
256	1	69	5.92E-06	8.43E-05	0.251
U_N	**Center x (cm)**	**Center y (cm)**	**sigma (cm)**	**least sq. difference**	**Kurtosis**
0.457	3.50	-0.60	15.00	0.201	-0.280

Table A-6: Size D Experimental conditions and results

Size AD

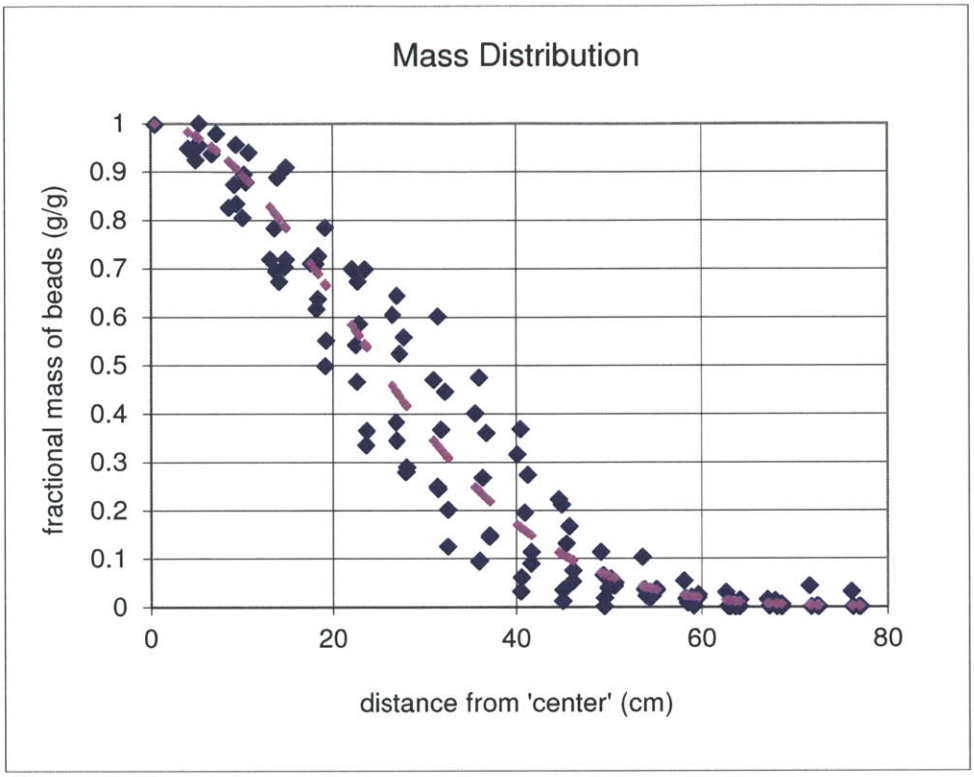

Figure A-7: Size AD sediment radial distribution

Particles Median diameter (μm)	**Mass released (kg)**	**Duration of release (s)**	**Q_b (m^3/s)**	**B (m^4/s^3)**	**N (1/s)**
159	1	78	5.23E-06	7.46E-05	0.254
U_N	**Center x (cm)**	**Center y (cm)**	**sigma (cm)**	**least sq. difference**	**Kurtosis**
0.236	-0.40	-2.80	21.30	0.303	-0.330

Table A-7: Size AD Experimental conditions and results

Size AE

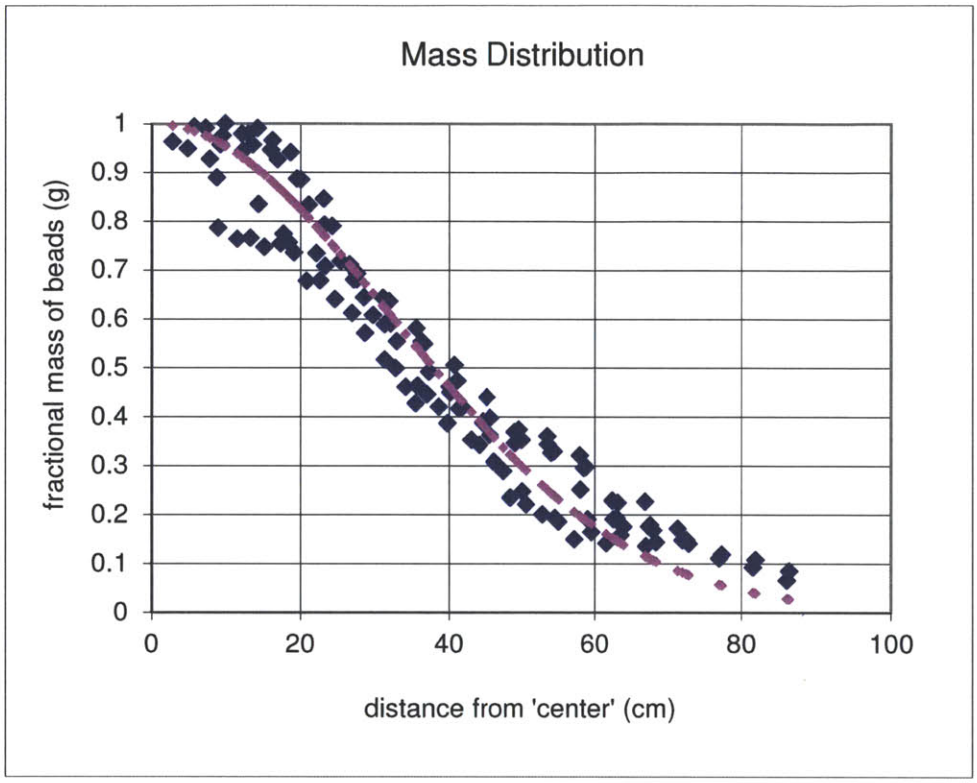

Figure A-8: Size AE sediment radial distribution

Particles Median diameter (μm)	**Mass released (kg)**	**Duration of release (s)**	**Q_b (m^3/s)**	**B (m^4/s^3)**	**N (1/s)**
120	1	94	4.34E-06	6.19E-05	0.26
U_N	**Center x (cm)**	**Center y (cm)**	**sigma (cm)**	**least sq. difference**	**Kurtosis**
0.159	-9.50	-5.30	32.20	0.094	-0.235

Table A-8: Size AE Experimental conditions and results

Size AG(1)

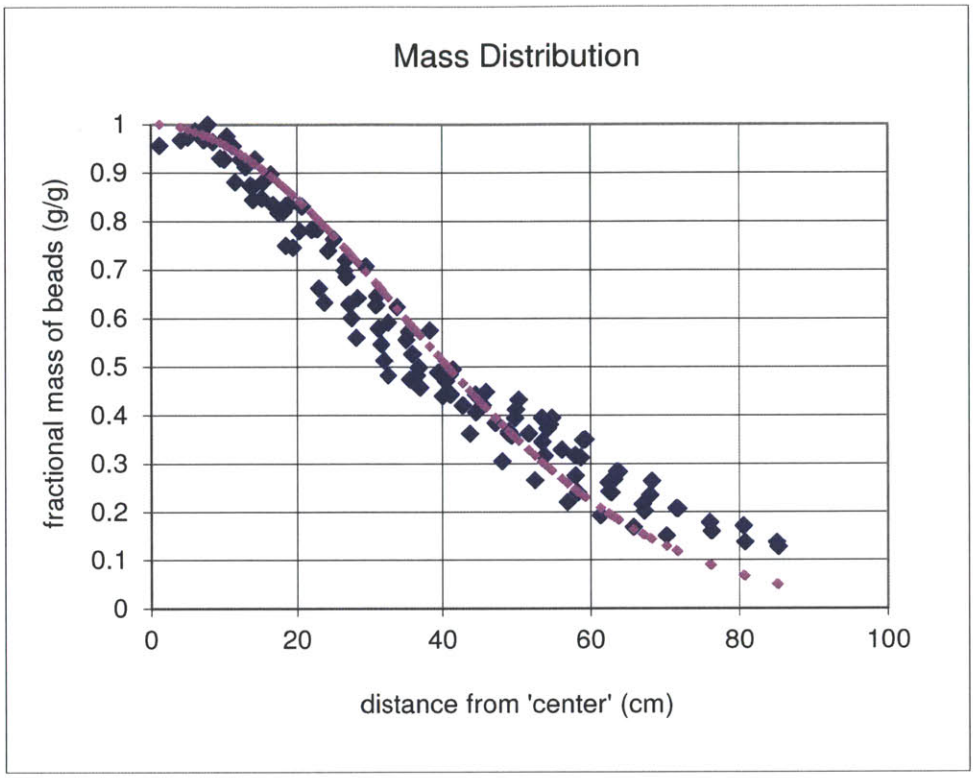

Figure A-9: Size AG(1) sediment radial distribution

Particles Median diameter (μm)	Mass released (kg)	Duration of release (s)	Q_b (m^3/s)	B (m^4/s^3)	N (1/s)
89	1	135	3.02E-06	4.31E-05	0.258
U_N	**Center x (cm)**	**Center y (cm)**	**sigma (cm)**	**least sq. difference**	**Kurtosis**
0.106	-8.50	-3.60	34.60	0.053	-0.245

Table A-9: Size AG(1) Experimental conditions and results

Size AG(2)

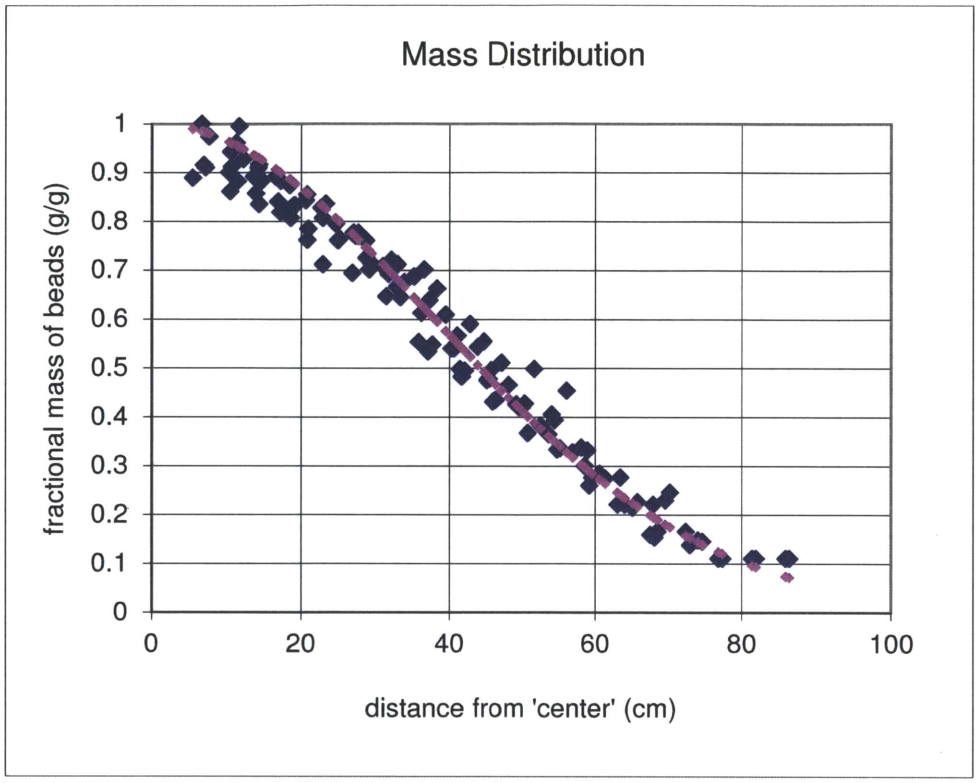

Figure A-10: Size AG(2) sediment radial distribution

Particles Median diameter (μm)	**Mass released (kg)**	**Duration of release (s)**	**Q_b (m^3/s)**	**B (m^4/s^3)**	**N (1/s)**
89	1	125	3.27E-06	4.65E-05	0.253
U_N	**Center x (cm)**	**Center y (cm)**	**sigma (cm)**	**least sq. difference**	**Kurtosis**
0.105	9.20	-8.00	37.60	0.026	-0.188

Table A-10: Size AG(2) Experimental conditions and results

Size AG(3)

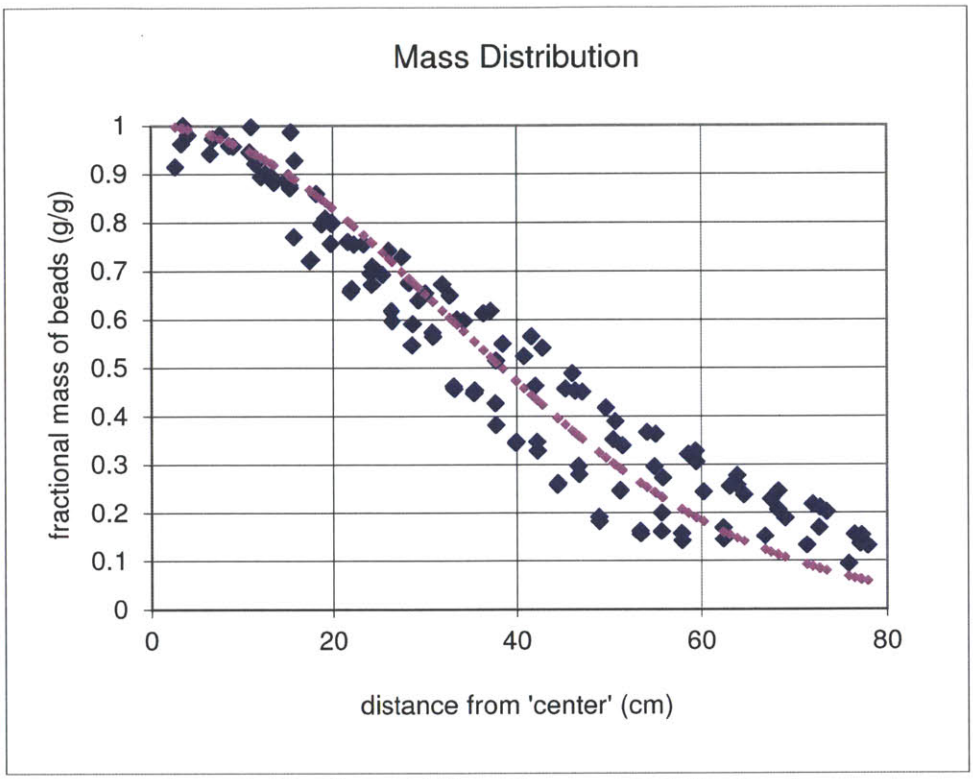

Figure A-11: Size AG(3) sediment radial distribution

Particles Median diameter (μm)	Mass released (kg)	Duration of release (s)	Q_b (m^3/s)	B (m^4/s^3)	N (1/s)
89	1	130	3.14E-06	4.48E-05	0.261
U_N	**Center x (cm)**	**Center y (cm)**	**sigma (cm)**	**least sq. difference**	**Kurtosis**
0.105	0.40	10.10	32.60	0.086	-0.198

Table A-11: Size AG(3) Experimental conditions and results

Size AH

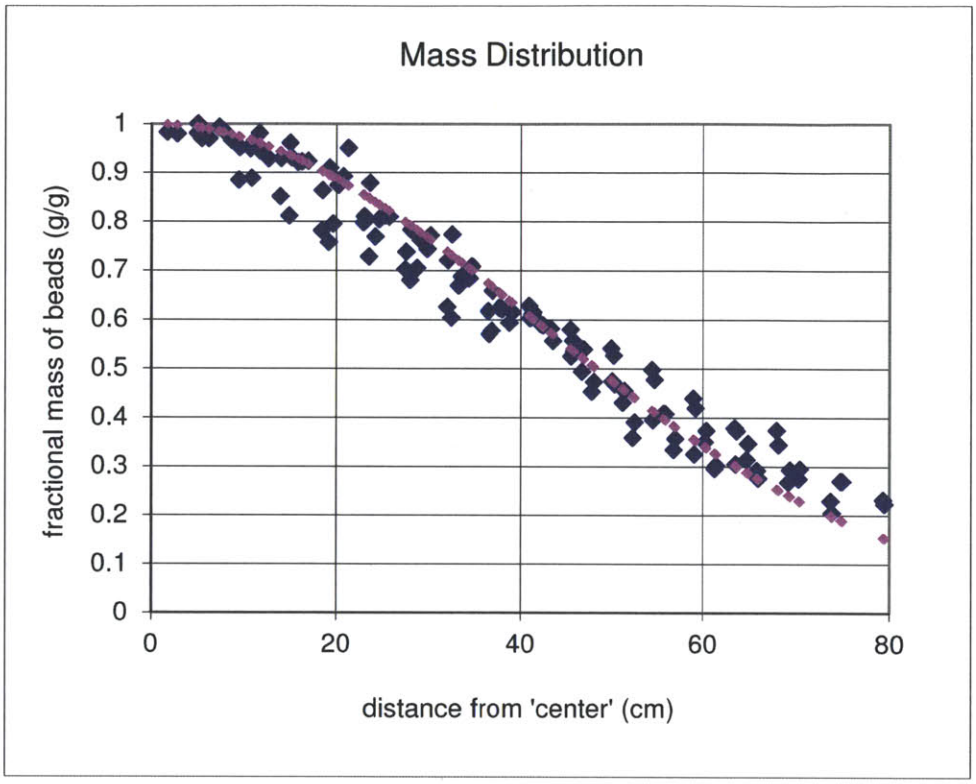

Figure A-12: Size AH sediment radial distribution

Particles Median diameter (μm)	Mass released (kg)	Duration of release (s)	Q_b (m^3/s)	B (m^4/s^3)	N (1/s)
67.5	1	210	1.94E-06	2.77E-05	0.254
U_N	**Center x (cm)**	**Center y (cm)**	**sigma (cm)**	**least sq. difference**	**Kurtosis**
0.074	2.80	-2.20	41.00	0.029	-0.357

Table A-12: Size AH Experimental conditions and results

A.2. Experiments with two different bead sizes

Size B&D

Mass of each size released (kg)	Duration of release (s)	Q_b (m^3/s)	B (m^4/s^3)	N (1/s)
0.5	50	4.08E-06	5.82E-05	0.256

Table A-13: Size B&D Experimental conditions

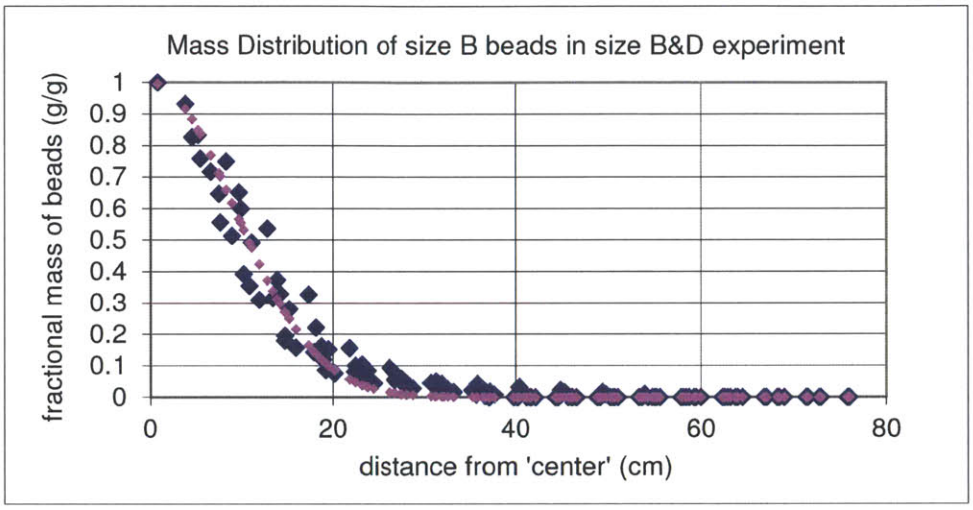

Figure A-13: Size B sediment radial distribution for experiment with size B&D beads

U_N	Center x (cm)	Center y (cm)	sigma (cm)	least sq. difference
1.198	-3.80	2.90	9.10	0.806

Table A-14: Size B Experimental results for experiment with size B&D beads

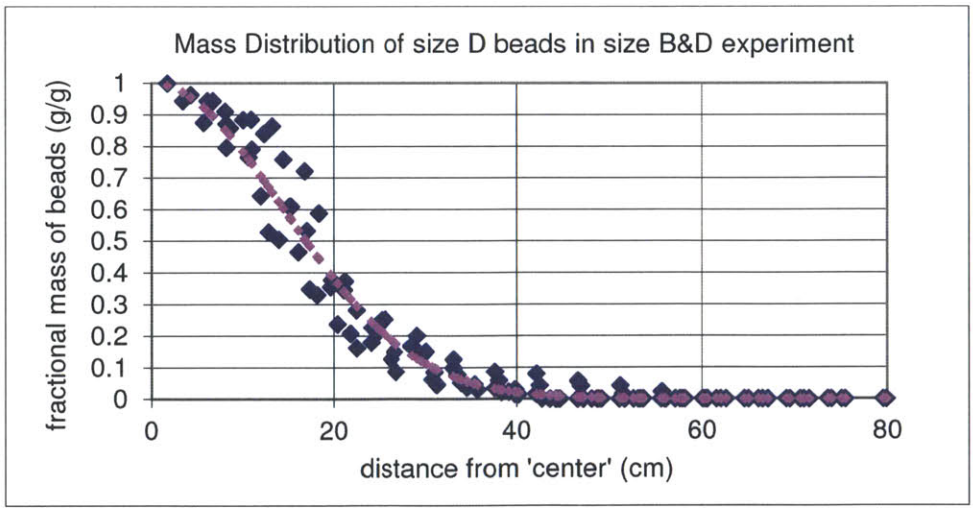

Figure A-14: Size D sediment radial distribution for experiment with size B&D beads

U_N	Center x (cm)	Center y (cm)	sigma (cm)	least sq. difference
0.499	-3.00	5.60	14.40	0.162

Table A-15: Size D Experimental results for experiment with size B&D beads

Size B&AG(1)

Mass of each size released (kg)	Duration of release (s)	Q_b (m^3/s)	B (m^4/s^3)	N (1/s)
0.5	60	3.40E-06	4.85E-05	0.254

Table A-16: Size B&AG(1) Experimental conditions

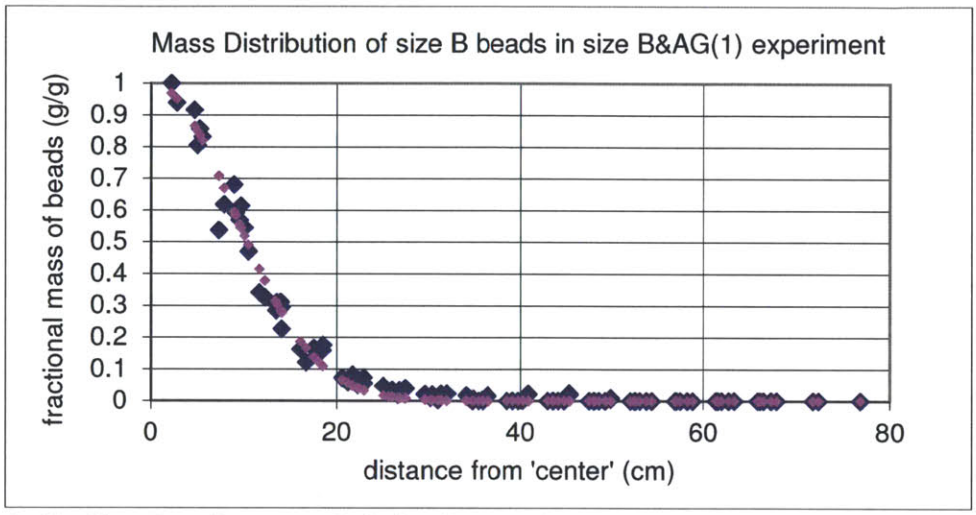

Figure A-15: Size B sediment radial distribution for experiment with size B&AG(1) beads

U_N	Center x (cm)	Center y (cm)	sigma (cm)	least sq. difference
1.254	-4.80	-0.30	8.80	0.386

Table A-17: Size B Experimental results for experiment with size B&AG(1) beads

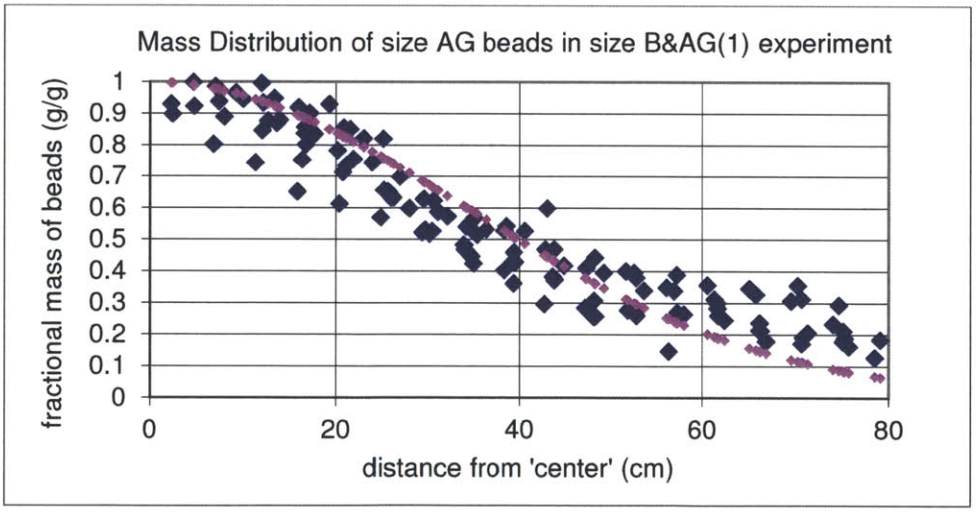

Figure A-16: Size AG sediment radial distribution for experiment with size B&AG(1) beads

U_N	Center x (cm)	Center y (cm)	sigma (cm)	least sq. difference
0.103	1.70	-9.40	33.90	0.033

Table A-18: Size AG Experimental results for experiment with size B&AG(1) beads

Size B&AG(2)

Mass of each size released (kg)	Duration of release (s)	Q_b (m^3/s)	B (m^4/s^3)	N (1/s)
0.5	62	3.29E-06	4.69E-05	0.255

Table A-19: Size B&AG(2) Experimental conditions

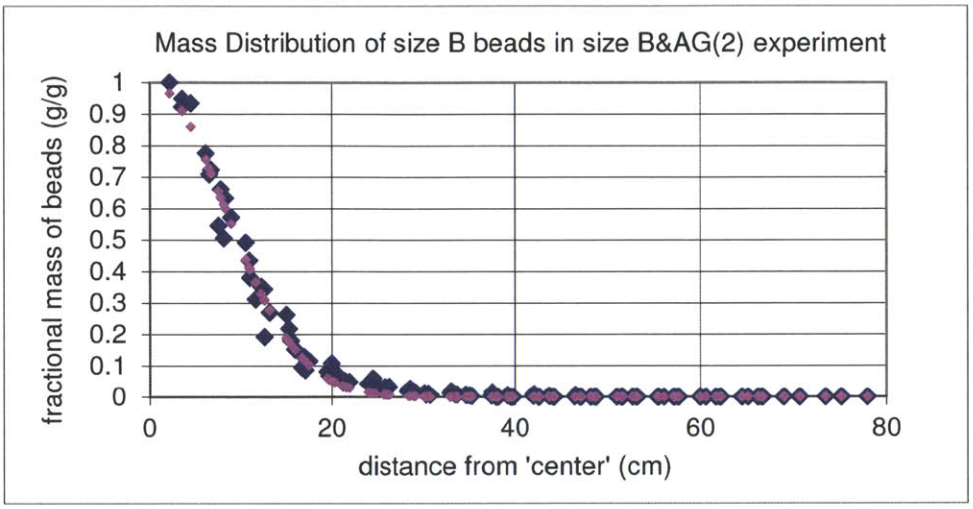

Figure A-17: Size B sediment radial distribution for experiment with size B&AG(2) beads

U_N	Center x (cm)	Center y (cm)	sigma (cm)	least sq. difference
1.265	-1.40	-0.80	8.20	0.352

Table A-20: Size B Experimental results for experiment with size B&AG(2) beads

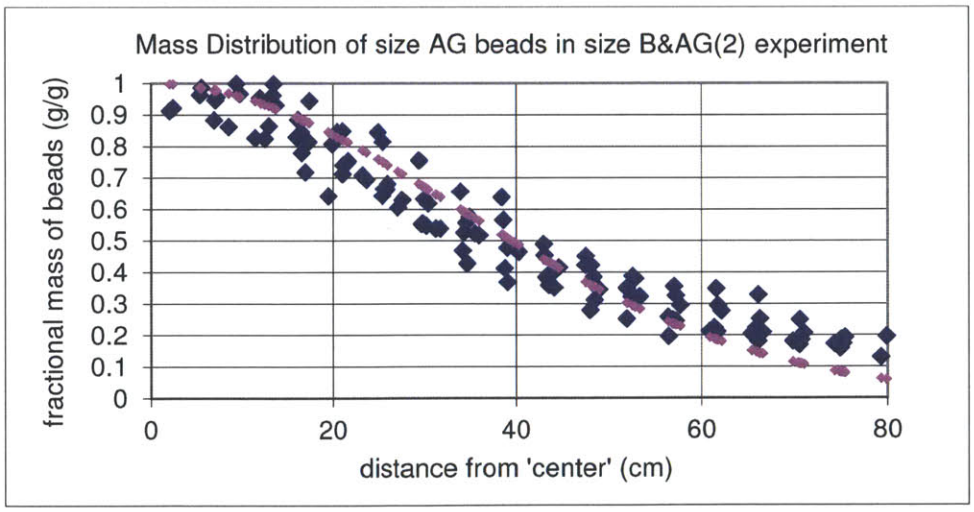

Figure A-18: Size AG sediment radial distribution for experiment with size B&AG(2) beads

U_N	Center x (cm)	Center y (cm)	sigma (cm)	least sq. difference
0.104	2.50	-9.30	33.60	0.026

Table A-21: Size AG Experimental results for experiment with size B&AG(2) beads

Size B&AG(3)

Mass of each size released (kg)	Duration of release (s)	Q_b (m^3/s)	B (m^4/s^3)	N (1/s)
0.5	57	3.58E-06	5.10E-05	0.257

Table A-22: Size B&AG(3) Experimental conditions

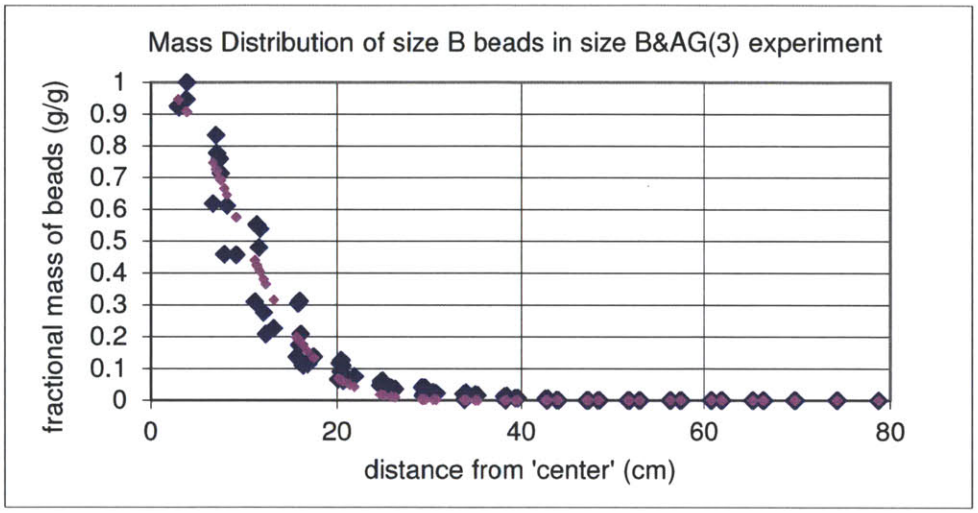

Figure A-19: Size B sediment radial distribution for experiment with size B&AG(3) beads

U_N	Center x (cm)	Center y (cm)	sigma (cm)	least sq. difference
1.238	-2.20	-0.60	8.70	1.033

Table A-23: Size B Experimental results for experiment with size B&AG(3) beads

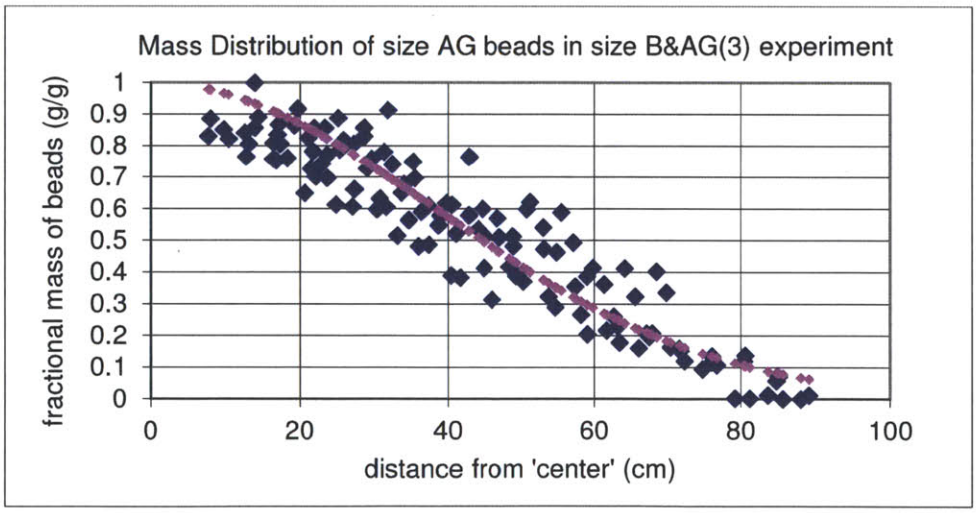

Figure A-20: Size AG sediment radial distribution for experiment with size B&AG(3) beads

U_N	Center x (cm)	Center y (cm)	sigma (cm)	least sq. difference
0.102	-10.00	-19.00	38.00	0.025

Table A-24: Size AG Experimental results for experiment with size B&AG(3) beads

Size D&AG

Mass of each size released (kg)	Duration of release (s)	Q_b (m^3/s)	B (m^4/s^3)	N (1/s)
0.5	70	2.92E-06	4.16E-05	0.255

Table A-25: Size D&AG Experimental conditions

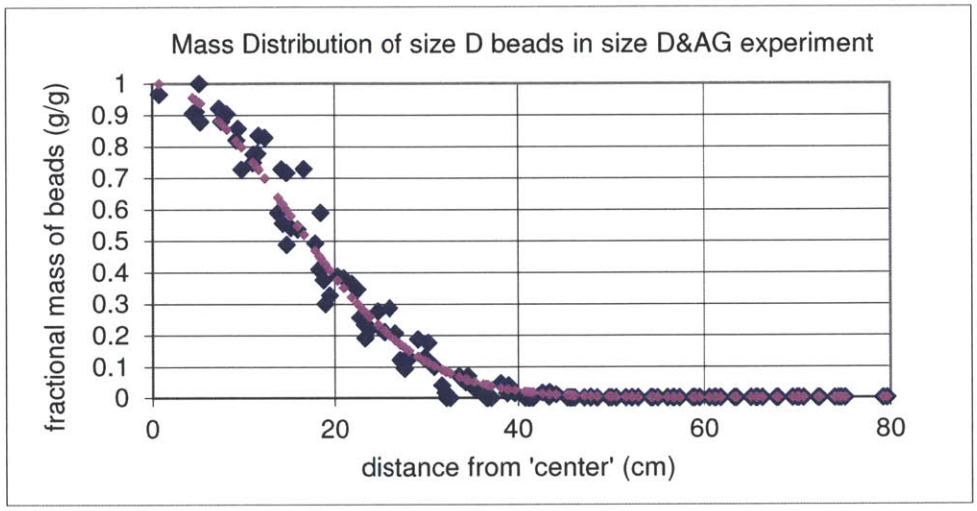

Figure A-21: Size D sediment radial distribution for experiment with size D&AG beads

U_N	Center x (cm)	Center y (cm)	sigma (cm)	least sq. difference
0.543	-2.60	-6.50	14.50	0.133

Table A-26: Size D Experimental results for experiment with size D&AG beads

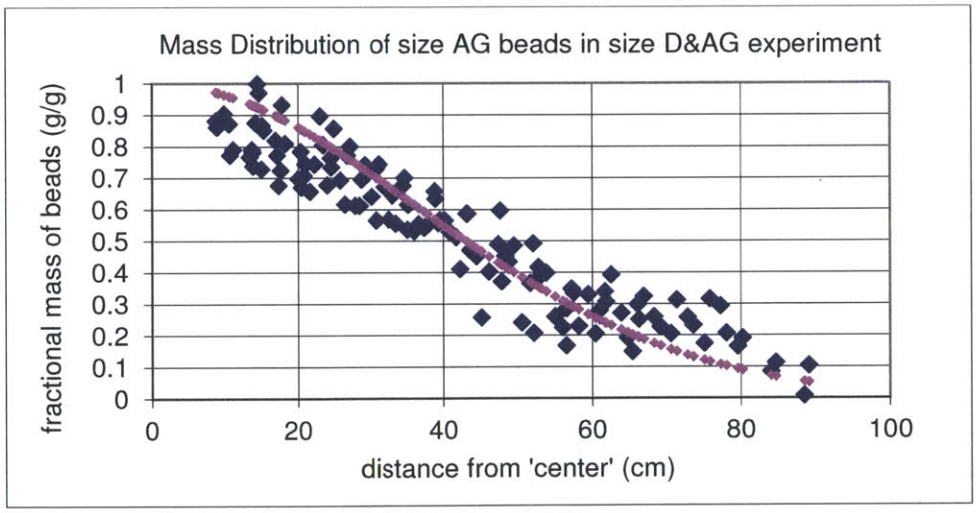

Figure A-22: Size AG sediment radial distribution for experiment with size D&AG beads

U_N	Center x (cm)	Center y (cm)	sigma (cm)	least sq. difference
0.107	-11.60	-11.00	36.60	0.012

Table A-27: Size AG Experimental results for experiment with size D&AG beads

Reference

[1] Adams, E. E., Golomb, D., Zhang, X. Y., & Herzog, H. J. (1995). Confined release of CO2 into shallow sea water. *Direct Ocean Disposal of Carbon Dioxide*, pages 153–164. TERRAPUB, Toyko.

[2] Alendal, G., Drange, H. (2001). Two-phase, near-field modeling of purposefully released CO_2 in the ocean. *Journal of Geophysical Research, 106(C1),* 1085-96.

[3] Asaeda, T., & Imberger, J. (1993). Structure of bubble plumes in linearly stratified environments. *Journal of Fluid Mechanics, 249*, 35-57.

[4] Auerbach, D. I., Caulfield, J. A., Adams, E. E., & Herzog, H. J. (1997). Impacts of ocean CO2 disposal on marine life: I. A toxicological assessment integrating constant-concentration laboratory assay data with variable-concentration field exposure. *Environmental Modeling and Assessment, 2*(4), 333-343.

[5] Bolin, B. (1995). Climate Change 1995. IPCC Second Assessment: Synthesis of scientific-technical information relevant to interpreting Article 2 of the UNFCCC, Technical report, Intergov. Panel Climate Change, New York.

[6] Cardoso, S. S. S., & Woods, A. W. (1993). Mixing by a turbulent plume in a confined stratified region. *Journal of Fluid Mechanics, 250*, 277-305.

[7] Caulfield, J. A., Adams, E. E., Auerbach, D. I., & Herzog, H. J. (1997). Impacts of ocean CO2 disposal on marine life: II. probabilistic plume exposure model used with a time-varying dose-response analysis. *Environmental Modeling and Assessment, 2*(4), 345-353.

[8] Chen, C. J., & Rodi, W. *Vertical Turbulent Buoyant Jets - A Review of Experimental Data.* Pergamon Press, 1980.

[9] Chen, F., & Yapa, P. D. (2003). A model for simulating deepwater oil and gas blowouts - part II: Comparison of numerical simulations with "deepspill" field experiments. *Journal of Hydraulic Research, 41*(4), 353-365.

[10] Chow, A. C. (2004). Effects of buoyancy source composition on multiphase plume behavior in stratification. S.M. thesis, Massachusetts Institute of Technology.

[11] Clift, R., Grace, J. R., and Weber, M. E. (1978). *Bubbles, drops, and particles*, Academic, New York.

[12] Crounse, B. C., Wannamaker, E. J., & Adams, E. E. (2007). Integral model of a multiphase plume in quiescent stratification. *Journal of Hydraulic Engineering, 133*(1), 70-76.

[13] Dietrich, W. E. (1982). Settling Velocity of Natural Particles. *Water Resources Research. 18(6):* 1615-1626.

[14] Dobran, F. *Volcanic Processes: Mechanism in Material Transport.* Kluwer Academic/Plenum Publishers, 1997.

[15] Elliot, A. J., Hurford, N., and Penn, C. J. (1986). ''Shear diffusion and the spreading of oil slicks.'' *Marine Pollution Bulletin*, 17(7), 308–313.

[16] Fischer, H. B., List, E. G., Koh, R. C. Y., Imberger, J. & Brooks, N.H. (1979). *Mixing in Inland and Coastal Waters*, Academic Press, New York, NY.

[17] Frias-Torres, S., & Bostater, C. R. (2011). Potential impacts of the deepwater horizon oil spill on large pelagic fishes. Paper presented at the *Proceedings of SPIE - the International Society for Optical Engineering, , 8175*

[18] Haberman, W. L., and Morton, R. K. (1954). ''An experimental study of bubbles moving in liquid.'' *Proc.*, ASCE, New York, 387.

[19] Haugen, P. and Drange, H. (1992). Sequestration of CO2 in the deep ocean by shallow injection. *Nature, 357(28),* 1065–1072.

[20] Herzog, H., Eliasson, B., & Kaarstad, O. (2000). Capturing greenhouse gases. *Scientific American, 282*(2), 72-79.

[21] Hill, D. F. (2002). General density gradients in general domains: The "two-tank" method revisited. *Experiments in Fluids, 32*(4), 434-440.

[22] Holder, G., Mokka, L., & Warzinski, R. (2001). Formation of hydrates from single phase aqueous solutions and implications for ocean sequestration of CO2. *Preprints of Spring 2000 National Meeting in San Diego, CA*. ACS Division of Fuel Chemistry.

[23] Holland, P. *Offshore blowouts: Causes and Control.* Gulf Pub. Co. 1997.

[24] Horel, A., Mortazavi, B., & Sobecky, P. A. (2012). Seasonal monitoring of hydrocarbon degraders in alabama marine ecosystems following the deepwater horizon oil spill. *Water, Air, and Soil Pollution, 223*(6), 3145-3154.

[25] Johansen, O., Rye, H., Melbye, A.G., Jensen, H. V., Serigstad, B., & Knutsen, T. (2001). Deep Spill JIP – Experimental Discharges of Gas and Oil at Helland Hansen – June 2000. Final Technical Report.

[26] Johansen, Ø., Rye, H., & Cooper, C. (2003). DeepSpill-field study of a simulated oil and gas blowout in deep water. *Spill Science and Technology Bulletin, 8*(5-6), 433-443.

[27] Knutzen, J. (1981). Effects of decreased pH on marine organisms. *Marine Pollution Bulletin, 12*(1), 25-29.

[28] Kobus, H. E. (1968). Analysis of the flow induced by air-bubble plueme systems. *Proceedings of the 11th International Conference of Coastal Engineering, London*, pages 1016–1031. ASCE.

[29] Kujawinski, E. B., Kido Soule, M. C., Valentine, D. L., Boysen, A. K., Longnecker, K., & Redmond, M. C. (2011). Fate of dispersants associated with the deepwater horizon oil spill. *Environmental Science and Technology, 45*(4), 1298-1306.

[30] Leitch, A. M., & Baines, W. D. (1989). Liquid volume flux in a weak bubble plume. *Journal of Fluid Mechanics, 205*, 77-98.

[31] Lessard, R. R., & DeMarco, G. (2000). The significance of oil spill dispersants. *Spill Science and Technology Bulletin, 6*(1), 59-68.

[32] Lin, Q., & Mendelssohn, I. A. (2012). Impacts and recovery of the deepwater horizon oil spill on vegetation structure and function of coastal salt marshes in the northern gulf of mexico. *Environmental Science and Technology, 46*(7), 3737-3743.

[33] Liro, C. R., Adams, E. E., & Herzog, H. J. (1992). Modeling the release of CO2 in the deep ocean. *Energy Conversion and Management, 33*(5-8), 667-674.

[34] McCutcheon, S. C., Martin, J. L. and Barnwell, T. O. J. *Handbook of Hydrology*. McGraw-Hill, New York, 1993.

[35] McDougall, T. J. (1978). Bubble plumes in stratified environments. *Journal of Fluid Mechanics. 85(4),* 655-672.

[36] Milgram, J. H. (1983). Mean flow in round bubble plumes. *Journal of Fluid Mechanics, 133*, 345-376.

[37] Nakanishi, N., Ohsumi, T., & Shitashima, K. (1994). Sequestering of CO2 in a deep ocean. Technical Report, Central Research Insitute of Electric Power Industry, 1646 Abiko, Abiko-City, Chiba 270-11, Japan.

[38] Rau, G. H., & Caldeira, K. (1999). Enhanced carbonate dissolution: A means of sequestering waste CO2 as ocean bicarbonate. *Energy Conversion and Management, 40*(17), 1803-1813.

[39] Ruggaber, G. J. (2000). Dynamics of particle clouds related to open-water sediment disposal. PhD thesis, Massachusetts Institute of Technology.

[40] Sato, T., Abe, S., & Miyata, H. (1998). Numerical simulation of droplet flow with mass transfer through interface. *Proceedings of FEDSM 1998 ASME Fluids Engineering Division Summer Meeting, Washington, DC.*

[41] Sato, T., Kajishima, T., & Naguosa, R. (2000) CO2 sequestration at sea by gas-lift system of shallow injection and deep releasing. *Environmental Science and Technology, 34*, 4140–4145.

[42] Sparks, R. S. J., Bursik, M. I., Carey, S. N., Gilbert, J. S., Glaze, L. S., Sigurdsson, H., & Woods, A. W. *Volcanic Plumes*. Wiley, 1997.

[43] Socolofsky, S.A. (2001). Laboratory experiments of multi-phase plumes in stratification and crossflow. PhD thesis, Massachusetts Institute of Technology.

[44] Socolofsky, S. A., & Adams, E. E. (2002). Multi-phase plumes in uniform and stratified crossflow. *Journal of Hydraulic Research, 40*(6), 661-672.

[45] Socolofsky, S. A., & Adams, E. E. (2005). Role of slip velocity in the behavior of stratified multiphase plumes. *Journal of Hydraulic Engineering, 131*(4), 273-282.

[46] Socolofsky, S. A., Adams, E. E., & Sherwood, C. R. (2011). Formation dynamics of subsurface hydrocarbon intrusions following the deepwater horizon blowout. *Geophysical Research Letters, 38*(9)

[47] Tacke, K. H., Schubert, H. G., Weber, D. J., & Schwerdtfeger, K. (1985). Characteristics of round vertical gas bubble jets. *Metallurgical Transactions B, 16*(2), 263-275.

[48] Takemura, F., and Yabe, A. (1999). ''Rising speed and dissolution rate of a carbon dioxide bubble in slightly contaminated water.'' *Journal of Fluid Mechanics*, Cambridge, U.K., 378, 319–334.

[49] Topham, D. R. (1975). Hydrodynamics of an oilwell blowout, Technical Report 33, Baufort Sea, Institute of Ocean Sciences, Sidney, B.C., Canada.

[50] Turner, J. S. (1986). Turbulent entrainment: the development of the entrainment assumption, and its application to geophysical flows. *Journal of Fluid Mechanics, 173*, 431-471.

[51] Warzinski, R. P., Lynn, R. J., & Holder, G. D. (2000). The impact of CO2 clathrate hydrate on deep ocean sequestration of CO2: experimental observations and modeling results. *Annals of the New York Academy of Sciences, 912*, 226–234.

[52] Wüest, A., Brooks, N. H., & Imboden, D. M. (1992). Bubble plume modeling for lake restoration. *Water Resources Research, 28*(12), 3235-3250.

[53] Yapa, P., & Chen, F. (2004). Behavior of oil and gas from deepwater blowouts. *Journal of Hydraulic Engineering, 130*(6), 540-553.

[54] Yapa, P. D., Zheng, L., & Nakata, K. (1999). Modeling underwater oil/gas jets and plumes. *Journal of Hydraulic Engineering, 125*(5), 481-491.

[55] Zheng, L., & Yapa, P. D. (2000). Buoyant velocity of spherical and nonspherical bubbles/droplets. *Journal of Hydraulic Engineering, 126*(11), 852-854.

[56] Zheng, L., Yapa, P. D., & Chen, F. (2003). A model for simulating deepwater oil and gas blowouts - part I: Theory and model formulation. *Journal of Hydraulic Research, 41*(4), 339-351.